JOURNAL OF MATERIALS SCIENCE 33 (1998) 4267–4285

Carrier-induced dynamic strain effects in semiconductor nanocrystals

XUE-SHU ZHAO, YU-RU GE*, XIN ZHAO‡
Departments of Material Science and Engineering, Chemistry and Electric Engineering,‡ Rensselaer Polytechnic Institute, Troy, NY 12180, USA*
Email: Zhaox2@rpi.edu

In this paper, we reveal, for the first time, the basic nature of electron–phonon interaction in semiconductor nanocrystals. On the basis of the experimental results on GaAs, GaP, Si nanocrystals, and porous silicon, we further prove that the carrier-induced dynamic strain effect (CIDSE) is a common feature in solids, which plays an extremely important role on the electronic and optical properties of semiconductor nanocrystals. The optical transitions in semiconductor nanocrystals are dominated by multiphonon-assisted electronic transition processes. Nanocrystals with direct-gap and a large pressure coefficient for the band gap (as GaAs) no longer show band-edge emission due to the intrinsic strong electron – long wavelength anharmonic acoustic phonon coupling. Nanocrystals with an indirect-gap show a carrier-induced dynamic Jahn–Teller effect and two fairly strong intrinsic emission bands. Most of the open questions in the semiconductor nanocrystal field, including porous silicon, can be consistently explained by the carrier-induced dynamic strained quantum dot model.

1. Introduction

The electronic and optical properties of semiconductor nanocrystals have received significant attention from both technology applications and fundamental science in recent years. Research in the nanocrystal field has been considerably stimulated by observation of the strong light emission from porous silicon [1]. Since semiconductor nanocrystals fall into the quantum size region, quantum confinement may play an important role in their electronic and optical properties. When nanocrystals become smaller than the Bohr radius of a free exciton in bulk semiconductors, their electronic wave functions experience three-dimensional quantum confinement due to the quantum dot boundary. Quantum confinement will transform the continuous bands of bulk semiconductors into discrete levels with high oscillator strength, which shift to higher energies with decreasing nanocrystal size [2–5].

Numerous theoretical and experimental studies on II–VI, IV and III–V semiconductor nanocrystals have confirmed that the blue shift of the lowest energy optical transition of semiconductor nanocrystals is dominated by quantum confinement [6–8]. However, quantitative prediction of the shift of the exciton energy with particle size has been an outstanding problem for a decade. In principle, the effective-mass model should be a valid approximation for predicting the confined energy for band edges. However, the effective-mass model always overestimates the confinement energy [9]. On the other hand, experimental results on all kinds of semiconductor nanocrystals (including porous silicon) show a number of common features that are in sharp contrast to the predictions of the quantum confinement model for a free exciton. These anomalous optical properties observed in the semiconductor nanocrystal field specifically include: extremely long radiative lifetimes of photo-carriers [10], broad absorption and emission spectra [11], large Stokes shift [12], soft vibrational modes [13], and much higher critical pressure for phase transitions [14, 15], as well as enhanced luminescence from deep level defects as crystallites are made smaller [16] and so on. Therefore, many other models have been proposed as a modification or substitution for the quantum confinement model. Some of these are the core model [17], surface model [18], core and surface mixed model [17], phonon confinement model [19], the polarization model [12], etc. However, every one of them can at best quantitatively describe only some of the above characteristics of semiconductor nanocrystals.

Obviously, all these open questions above are connected with lattice relaxation as electronic transition occurs. In understanding the basic nature of the quantum confinement system, electron–lattice interaction in such systems becomes of utmost importance. Quantum confinement naturally leads to energy confinement, which means that most of the energy for excited free carriers is confined to the tiny volume of a nanocrystal. For this reason, semiconductor nanocrystals have high energy density under excitation. It is just this energy confinement for excited free carriers that makes the optical and electronic properties of

semiconductor nanocrystals show a number of the "anomalous" properties mentioned above. However, all models proposed so far in the nanocrystal field totally ignore the energy of the excited electrons and holes themselves, and treat a nanocrystal as a rigid cavity. The key to the importance of excited free carriers to the optical properties of semiconductor nanocrystals is the fact that a single excitation in a Si nanocrystal with diameter of 2 nm corresponds to an increase of about 10^{20} eV cm^{-3} in the free-energy density, which will include about a 20 kbar tensile stress in the Si nanocrystal, provided that the Si nanocrystal has reached its excited equilibrium state. Thus, the dynamic strain induced by excited free carriers in semiconductor nanocrystals greatly changes the optical properties predicted by the quantum confinement model. According to the total-energy principle, an increase of free energy in a crystal system will naturally lead to an increase in lattice relaxation. The dynamic strain induced by excited free carriers will break the orthogonality of vibronic wave functions between excited states and the ground state. Therefore, the optical properties of semiconductor nanocrystals are dominated by multiphonon-assisted optical transition processes [13, 20, 21].

We have proposed on the basis of our previous studies on Si and GaAs nanocrystals that the dynamic strain induced by excited free carriers is a common feature of all confined systems. We predicted that indirect-gap nanocrystals, such as Si, Ge and GaP, would be more likely to exhibit the carrier-induced Jahn–Teller effect due to the degenerate lowest excited levels. We have found that quantum confinement can transform the band gap of GaAs nanocrystals from direct to indirect as the particle size becomes smaller than 5.0 nm [13, 20]. This has also been demonstrated in a recent theoretical calculation [22]. When this transformation occurs, the optical properties of GaAs nanocrystals undergo a significant change.

In this paper we will further prove, on the basis of experimental results on GaAs, GaP, Si nanocrystals, and porous silicon, that CIDSE is the intrinsic common feature in solids, which plays an extremely important role on the electronic and optical properties of semiconductor nanocrystals. The optical properties of semiconductor nanocrystals are dominated by multiphonon-assisted electronic transition processes. Most of the open questions in semiconductor nanocrystals, including porous silicon, can be consistently explained by the carrier-induced strained quantum dot model.

However, carrier-induced strain, or the lattice relaxation effect, presently is not an accepted mechanism in understanding the optical properties in solids, even in strong excitation cases. For this reason, we give a more detailed argument about the carrier-induced dynamic strain effects in the following section.

1.1. Carrier-induced dynamic strain effects

In the early 1960s, Keys had found that free carriers in Si and Ge bulk materials can decrease the elastic constants for shear strain due to an increase of free energy. The decrease of the elastic constant is proportional to the cubic root of free carrier density. For example, 0.06% arsenic impurity in Ge produces a 5.5% decrease in C_{44} [23].

In order to show the CIDSE in nanocrystals, we begin with Huang's classic theory for electron–lattice interaction in solids [24, 25]. In an electron–lattice interaction system, one-electronic total Hamiltonian, H_t is

$$H_t = H_e + H_L + H_{Le} \tag{1}$$

where H_e, H_L and H_{Le} represent the electronic, lattice vibrational, and electron–lattice interaction Hamiltonians, respectively. In the adiabatic approximation, the total wave function is approximately of vibronic form

$$\Psi_{in}(x, Q) = \varphi_i(x, Q) X_{in}(Q) \tag{2}$$

where $X_{in}(Q)$ is a wave function for vibrational state, n, in the electronic level, i; and x and Q represent the electron co-ordinate and the lattice normal co-ordinate, respectively, $\varphi_i(x, Q)$ is an eigenfunction of the one-electron Schrödinger equation including the electron–lattice interaction

$$[H_e(p, x) + H_{Le}(x, Q)]\varphi_i(x, Q) = E_i(Q)\varphi_i(x, Q) \tag{3}$$

where both the electronic wave function and eigenvalue, $E_i(Q)$, are dependent on the ionic positions. The full adiabatic vibrational Schrödinger equation for an electron in the level i is

$$[H_L(p, Q) + E_i(Q)] X_{in}(Q) = E^t_{in} X_{in}(Q) \tag{4}$$

where $X_{in}(Q)$ are the harmonic oscillator wave functions, and E^t_{in} is the total energy, electron plus vibrational $E_i(Q)$ is the eigenvalue of the one-electron Schrodinger equation (3), which plays the role of additive potential in the vibrational equation. This additive potential will displace the origins for all harmonic vibrators in electronic level i, provided that an excited electron is in the level i. The configuration-co-ordinate diagram (Fig. 1) for describing the electron–lattice interaction is just based on this total energy equation. In the harmonic approximation, the vibrational Hamiltonian can be written as

$$H_L = \sum_s \tfrac{1}{2}(-\hbar^2 \partial^2/\partial Q_s^2 + \omega_s Q_s^2) \tag{5}$$

For the sake of simplicity, in the following discussion we assume that all vibrational models have the same frequency, ω_0. The electronic eigenvalue, $E_i(Q)$, can be expanded in terms of the normal co-ordinates to the line term

$$E_i(Q) = E_i^o + (1/N)^{1/2} \sum_s \omega_o^2 \Delta_{is} Q_s \tag{6}$$

where E_i^o is the eigenvalue for one-electron Schrödinger equation, Equation 3, with $H_{Le} = 0$. Δ_{is} is the displacement of vibrational mode, Q_s, caused by an excited electron in energy level i. N is the total number of harmonic vibrators in the system. Then the vibrational equation becomes

$$\left\{E_i^o + \sum_s [\tfrac{1}{2}(-\hbar^2 \partial^2/\partial Q_s^2 + \omega_o^2 Q_s^2) + (1/N)^{1/2} \omega_o^2 \Delta_{is} Q_s]\right\} \times X_{in}(Q) = E^t_{in} X_{in}(Q) \tag{7}$$

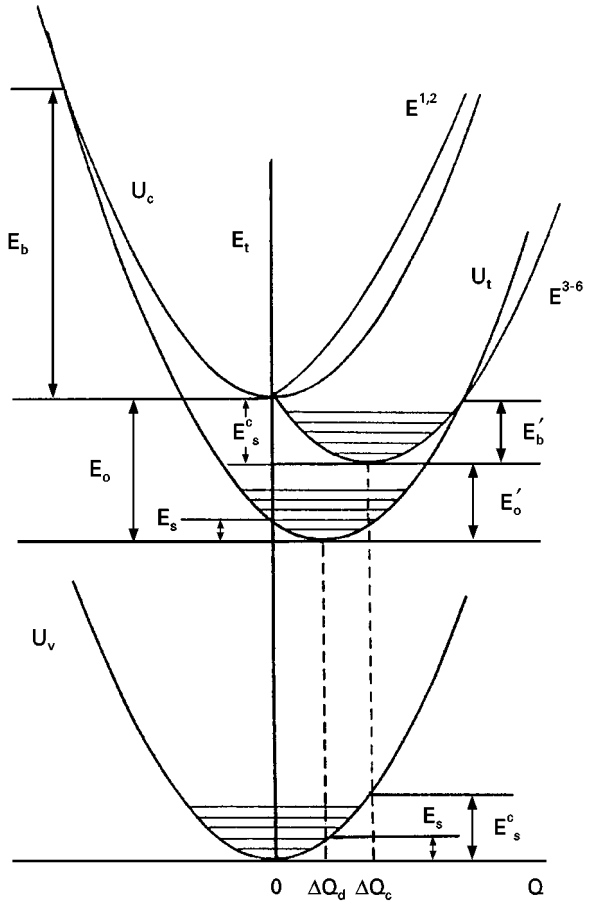

Figure 1 The configuration co-ordinate diagram for a Si nanocrystal, showing the total energy of the free electron, trapped electron and the free hole. U_c, U_v and U_t are the energy curves for the free electron, hole and bound electron. $E^{1,2}$ and E^{3-6} versus Q curves represent the split unstable excited states and energy-relaxed band-edge states. E_o and E'_o are the binding energy of a trapped electron before and after lattice relaxation. E_b and E'_b are the thermal barrier of deep level U_t before and after lattice relaxation. E^c_s and E_s are the Franck–Condon energies for conduction band and for trapped electronic state, respectively.

Introducing a new normal co-ordinate, $Q_{is} = Q_s + (1/N)^{1/2}\Delta_{is}$, the vibrational equation yields

$$\left[\sum_s \tfrac{1}{2}(-\hbar^2\partial^2/\partial Q_{is}^2 + \omega_o^2 Q_{is}^2) + E_i^o - 1/N\sum_s \tfrac{1}{2}\omega_o^2\Delta_{is}^2\right] \times X_{in}(Q) = E_{in}^t X_{in}(Q) \quad (8)$$

Comparing Equations 4 and 8 we find

$$E_i(Q) = E_i^o - 1/N\sum_s 1/2\,\omega_o^2\Delta_{is}^2 \quad (9)$$

where $1/N\sum_s 1/2\,\omega_o^2\Delta_{is}^2$ represents the energy shift of the one-electron, E_i^o, due to electron–lattice interaction. This quantity is often referred to as the Franck–Condon energy of electronic state i [26]. It is an useful conceptual aid to express the Franck–Condon energy in terms of the number of phonons involved in the electron–phonon coupling.

$$E_{FC} = S\hbar\omega_o \qquad S = 1/N\sum_s(\omega_o^2/2\hbar)\Delta_{is}^2 \quad (10)$$

The factor S is the electron–phonon coupling strength, which was first introduced by Huang and Rhys [24].

Now, the optical emission line shape for the electronic transition from excited state, i, with energy level E_i, to the ground state, g, with energy $E_g = 0$, is given by

$$F(E) = M_{gi}^2 \mathrm{Av}_n \sum_{n'}\prod_s [\langle X_{gn'}(Q_{gs})\,|\,X_{in}(Q_{is})\rangle]^2 \times \delta(E - E_i - p\hbar\omega_o) = M_{gi}^2 e^{-S}(S^p/p!) \quad (11)$$

where $M_{gi} = \langle\varphi_g(x, Q)\,|\,M\,|\,\varphi_i(x, Q)\rangle$ are the electric dipole matrix elements between electronic states i and g. $\prod$ represents the product of all harmonic vibrators. Av represents the statistical average of phonon state n in electronic state i. $e^{-S}(S^p/p!)$ results from the overlap integrates of the vibrational wave functions in electronic state g and i, and $p = \sum_s(n_s - n'_s)$ is the number of phonons involved in the transition. The term, e^{-S}, comes from the contribution of the zero phonon line. At high temperature this quantity becomes

$$e^{-S}(S^p/p!) = (\hbar\omega_o/4\pi S k_B T)^{1/2}\exp[-(p - S)^2\hbar\omega_o/4k_B TS] \quad (12)$$

which shows a Gaussian distribution with a half-width, $(k_B TS\hbar\omega_o)^{1/2}$, centred at $p = S$ [25, 26]. We present here only the outline of the classic theory about the electron–lattice interaction in solids. A more detailed analysis can be found in 24–26.

It is obvious that when the displacements of the harmonic vibrators induced by the excited electronic energy cannot be ignored, the vibrational wave functions in electronic states i and g are no longer orthogonal. Therefore, the transition of electrons from excited state i to ground state g will involve multi-phonon emission processes. The emission spectrum of the electronic transition becomes a Gaussian shape centred on $E^i(Q) - S\hbar\omega_o$ or $E_o^i - 2S\hbar\omega_o$. Here, $2S\hbar\omega$ is known as the Stokes shift between absorption and emission frequencies.

Now we can see that the electron–lattice interaction in solids originates from lattice strain (or lattice relaxation) caused by the excited electronic energy, and the lattice strain, in turn, results in a shift of the electronic energy level. The total energy equation, Equation 4, shows that as long as the electronic energy is changed, even when the perturbation that causes the electronic transition does not act directly on the lattice, multi-phonon emissions (or absorption) must occur, because the vibrational states cannot avoid being displaced [26]. We have to keep in mind that although a static strain can change the lattice symmetry and distribution of energy states for a crystal system, the optical transitions in a static strained crystal have to obey the selection rule of crystal momentum conservation. Only the dynamic strain induced by excited carriers can relax the selection rule of crystal momentum conservation and lead to multiphonon transition processes.

An excited free electron in a bulk semiconductor distributes its energy in a relatively large volume. The involved number of vibrational modes, N, is the order of the number of atoms in the volume of the cavity.

By the definition of S above, the displacements of vibrational modes in excited states are so small that the vibrational wave functions between the ground state and excited states will basically remain orthogonal. In this case, the bulk crystal can be approximately considered as a rigid cavity under weak excitation. Consequently, the line-shape function, Equation 11, is only involved with the electric dipole matrix elements of the Bloch wave functions between two band states. Since the Bloch functions between the different bands and wave vectors must satisfy the orthogonal condition, under a perturbation, the electronic transition between two bands is allowed only if the transition is performed at the same wave vector, $\boldsymbol{k}$, namely vertical transition. Since $\hbar\boldsymbol{k}$ has the similar property as classic momentum, $\hbar\boldsymbol{k}$ is usually referred to as crystal momentum. Thus, the electronic transition in crystals has to simultaneously satisfy the constraints for both energy and crystal momentum conservation. Since the momentum of a photon is quite small compared with the crystal momentum, the optical transition in direct-gap crystals basically satisfies the selection rule of crystal momentum conservation. Therefore, the optical processes in direct-gap crystals tend to show fairly high efficiency. In contrast, in indirect-gap crystals, the extrema of the conduction-band and valence-band occur at different points in $\boldsymbol{k}$-space. In principle, if the ions are fixed on their equilibrium lattice positions, the optical transitions between extrema in indirect-gap crystals are forbidden. However, as we have discussed above, the excited electron always create the dynamic lattice strain by releasing their energy to the lattice. The induced strain partially destroys the periodic potential. As a result, the strict orthogonality of the Bloch wave functions (or the constraint of crystal momentum conservation) is relaxed. In principle, any lattice strain or displacement can be expanded in terms of the normal coordinates of vibrational modes. That is, a lattice strain consists of a number of optical and acoustic phonons. Thus the electron, for example, in the conduction-band minimum, through interaction with lattice strain, will emit or absorb some phonon that has the momentum required for crystal momentum conservation. Then the electron performs the vertical transition between the two bands. It is thus seen that in the one-electron energy band model, indirect transition can be allowed only if the crystal periodic potential has to suffer a dynamic distortion in a relatively short range. For this reason, as an excited electron is bound to a deep defect, the short-range potential in such a centre will localize the electron in a tiny volume around the defect. That is, the partial energy of an excited electron is confined to the small volume around the defect. Thus, indirect transitions involving localized deep states in some cases are in competition with direct transition due to the strong electron–phonon coupling (for instance, the nitrogen isoelectronic traps in GaP semiconductors). Since the indirect transition is a second-order perturbation process, the optical transitions in indirect-gap crystals are usually considerably slower and much less efficient.

It is worth noting that the classic theory for electron–lattice interaction includes an assumption that the crystal system has already reached its new equilibrium state, as an excited electron lands at an excited state. In fact, the strength of electron–lattice interaction is not a constant dominated by the electronic and vibrational states in a system, but it mostly depends upon the conditions of the excited equilibrium state, which will be discussed below in more detail.

In a rigorous thermodynamic sense, the forbidden gap, E_g, of a semiconductor is properly defined as the standard chemical potential, μ, for an electron–hole pair created in the thermal equilibrium state [27]. As a chemical potential, E_g is equal to the increase in Gibbs' free energy, G, upon increasing the number of such pairs, N, by one at constant temperature and pressure. That is, $\mu = E_g = (\partial G/\partial N)_{T,P}$ [28, 29]. This is the exact form of energy used in the Fermi distribution function. From the thermodynamic relation $dG = V\,dP - S\,dT$, it is readily seen that for a reaction in which a change in Gibbs' free energy is involved, the equation above can be written as $(\partial \Delta G/\partial P)_T = \Delta V$ at constant temperature. This well known equation shows that the isothermal pressure dependence of ΔG measures a volume change, ΔV, under thermal equilibrium conditions. We deal here with the tensile strain case, where ΔG is the increase in the free energy upon excitation. ΔV must be the tensile strain of the volume for a nanocrystal, and ΔP represents the tensile stress that occurs in a nanocrystal. Assuming only one electron–hole pair is created and the lifetime of excited free carriers is long enough for the nanocrystal to reach its excited equilibrium state, we can estimate the volume change, ΔV, caused by increasing E_g in free energy in a nanocrystal with volume V_o. It will be a valid approximation to use the infinitesimal approach

$$\Delta V = (\partial \Delta G/\partial V)_T(\partial V/\partial P)_T \quad \text{hence } \Delta V^2 = E_g(K \times V_o) \tag{13}$$

where $K = -(\partial V/\partial P)_T/V$ is the compressibility ($K = 1.34 \times 10^{-5}$ and 1.02×10^5 Pa for bulk GaAs and Si, respectively).

The increase in volume of a nanocrystal must lead to an increase of the internal energy, which should be equal to the work performed by the nanocrystal during the tensile strain from V_o to V'. Following the method used by Born for calculating lattice energy [29], the work performed by the nanocrystal is $W = \int_{V_o}^{V'} P\,dV$, where $P \cong -(V - V_o)/KV_o$. Thus, the increase of the internal energy in the nanocrystal is $\Delta E = W = \Delta V^2/(2K \times V_o)$. By substituting Equation 13 into this equation, we find that at the equilibrium condition the increase in strain energy (internal energy) of the nanocrystal is $\Delta E = \frac{1}{2}E_g$, which is independent of volume for a closed system. This simple relation means that in order to support one electron–hole pair to stay at its thermal equilibrium state, the crystal requires another $\frac{1}{2}E_g$ energy to create the lattice strain. The stress occurring in the nanocrystal can be obtained by means of the well known thermodynamic equation, $\Delta P = -(d\Delta E/dV)_{T=0}$,

and hence

$$\Delta P = -(2\Delta E/KV_o)^{1/2} \quad \text{or} \quad \Delta P = -(E_g/KV_o)^{1/2} \tag{14}$$

The same equation also can be obtained in terms of Hooke's law [13]. Strictly, the stress occurring in a nanocrystal is a function of the increment in the internal energy density (or strain energy in this case).

It is thus seen from the arguments above that if there exists a forbidden band gap, E_g, in a semiconductor with V_o, the photon energy needed to excite one electron from the valence-band edge to the conduction-band edge is about $\frac{3}{2}E_g$, provided the excited free carriers have a long enough lifetime for the lattice to reach its excited equilibrium state (this is true for most kinds of semiconductor nanocrystals). The $\frac{1}{2}E_g$ energy of the photon is used to produce the lattice strain. The lattice strain, in turn, results in an energy relaxation for electronic levels and vibrational modes. The energy shift of the conduction-band edge can be expressed as $\Delta E_s^c = dE_g/dp \times \Delta P$, where dE_g/dp represents the pressure (or stress) coefficient for the band gap of the semiconductor, and $\Delta P = -(E_g/KV_o)^{1/2}$. As mentioned above, this energy relaxation is, in fact, just the Franck–Condon shift for the conduction-band edge. If we assume that the frequencies of the vibrational modes in excited states remain the same as those in the ground state, then the Franck–Condon shift is one-half of the Stokes shift. In fact, the vibrational modes that occur in nanocrystals are continuous modes rather than a single mode. In this case, the band edge relaxation (or the Franck–Condon shift) can be approximately written as $E_s^c = \sum_n S_n \hbar\omega_n$, where S_n is the Huang–Rhys electron–phonon coupling strength of the phonon with energy $\hbar\omega_n$, and the sum is over all modes involved in the coupling [30].

It is obvious that if there exist n_p such electron–hole pairs at the band edges and the crystal has reached its new equilibrium state, then the energy shift for the conduction-band edge should be $E_s^c = dE_g/dp \times (n_p E_g/KV_o)^{1/2}$ or $dE_g/dp \times (nE_g/K)^{1/2}$, where $n = n_p/V_o$, the density of electron–hole pairs. For instance, if a density of $n = 10^{14}\,\text{cm}^{-3}$ of electron–hole pairs is created by an excitation with photon energy of $\frac{3}{2}E_g$ in bulk GaAs, the carrier-induced stress and the energy shift for the conduction-band edge are -1.3×10^{-2} kbar and -0.14 meV, respectively. Thus, the carrier-induced strain effect is negligible at low excitation. However, if the density of excited electron–hole pairs is increased to $n = 5 \times 10^{17}\,\text{cm}^{-3}$, the two quantities above become -0.9 kbar and -10 meV, respectively. In this case, the energy shift of the conduction-band edge is just equal to the bonding energy of so-called electron-hole liquid drop in bulk GaAs. Now we can see that even in bulk crystals, the CIDSE cannot be ignored at the strong excitation case. In fact, it has been found in bulk crystals that the strong excitation always produces a strong stress that expands from the excited volume into the unexcited volume [31, 32].

As the crystallites are made smaller, the band gap (chemical potential) of the crystallites will be increased by quantum confinement. For the same density of the electron–hole pairs at the excited equilibrium state, the carrier-induced stress in nanocrystals will be much higher than that in the corresponding bulk crystal. As the photon energy, E_p, is in the range $E_g < E_p < \frac{3}{2}E_g$, the condition required for the excited equilibrium state is not achieved if only one electron–hole pair is excited. In this case, the energy relaxation for the band edge cannot be developed completely. Suppose there exists a density, n, for such electron–hole pairs in a nanocrystal at a steady excitation, then the energy of $n(1 - 2E_p/3E_g)$ electron–hole pairs will be used to create the lattice strain. The corresponding stress and the energy shift of the conduction-band edge in the nanocrystals are about $(\frac{2}{3}nE_p/K)^{1/2}$ and dE_g/dp $(\frac{2}{3}nE_p/K)^{1/2}$, respectively. As the photon energy of the excitation light is much higher than $\frac{3}{2}E_g$, the conduction-band edge will undergo an over relaxation, and the excited electrons at the conduction-band edge need more time to release their excess energy. Thus, the optimum emission for a nanocrystal with a band gap, E_g, can be achieved when the photon energy of the excitation light is close to $\frac{3}{2}E_g$. This dependence of emission efficiency on the photon energy of the excitation light has been observed in porous silicon and Si nanocrystals [33]. Now we can conclude that the electron–phonon coupling strength, S_n, is not a constant in nanocrystals, it depends directly on photon energy, excitation intensity, band gap (versus size), and pressure (or stress) rate for the band gap.

In Fig. 1 we show as an example the configuration co-ordinate diagram of silicon nanocrystals. Following the pioneer work on the capture cross-sections of defect states [34, 35], we use U_v and U_c to represent the total energy (electronic plus lattice) for free hole and free electron at band edges and the U_t versus Q curve for deep level states. The origin of normal co-ordinates for a nanocrystal is taken at the lattice equilibrium position. Silicon nanocrystals have six-fold degenerate levels at Δ points in the electronic Brillouin zone (BZ). The excited electrons in the six-fold degenerate levels will induce the uniaxial stress in the [1 0 0] direction [23], which will split the six-fold degenerate levels into the two up $E^{1,2}$ aligned along the stress direction (longitudinal valleys) and the four down E^{3-6} perpendicular to the stress axis (transverse valleys) [36, 37]. Their shifts, with respect to the weight of the six levels, are

$$\begin{aligned} E^{1,2} &= \tfrac{2}{3}F\Xi_u(S_{11} - S_{12}) \\ E^{3-6} &= -\tfrac{1}{3}F\Xi_u(S_{11} - S_{12}), \end{aligned} \tag{15}$$

where F is the stress induced by excited free carriers, Ξ_u is the shear strain deformation potential, and S_{11} and S_{12} are the elastic compliance constants. According to the Jahn–Teller theorem, only the lowest E^{3-6} levels are the energy relaxed stable states [30]. We refer to this energy splitting in indirect-gap nanocrystals as the carrier-induced dynamic Jahn–Teller effect. Therefore, indirect-gap nanocrystals should exhibit two intrinsic emission bands, as observed in porous Si and silicon nanocrystals. One is the high energy, fast emission band, and the other is the low energy, slow band-edge emission band [33]. For direct-gap

nanocrystals, E^{3-6} may simply represent the energy relaxation of the singlet Γ band edge.

The short-range nature of deep level states requires that the wave function of deep level centres must consist of contributions from the whole of k-space and from all bands. It is then no longer possible to associate a deep level with one of the conduction band or valence band extreme. For this reason, the deep centres in nanocrystals should be insensitive to quantum confinement. However, a number of experimental results have shown that most of the deep centres in semiconductor nanocrystals and porous Si do exhibit strong light emission [16]. An efficient emission defect centre in a semiconductor has to meet the requirements of both a small Stokes shift and a large capture cross-section. The well known equation for the thermal barrier energy of a defect centre shows that $E_b = (E_o - E_s)^2/4E_s$, the quantities in the equation as shown in Fig. 1. Obviously, it is impossible for a deep centre in bulk crystals to meet both requirements simultaneously. However, the case in nanocrystals is totally changed by the CIDSE. The large capture cross-section for the deep centre with a weak electron–phonon coupling can be achieved by band-edge relaxation. The energy relaxation of the deep level in the band gap is dependent on the relative positions of the defect and its neighbouring lattice atoms. If we assume that for a contraction relaxed ($\Delta Q < 0$) deep centre with its energy relaxation $E_s = E_s^c$ and an outward relaxed ($\Delta Q > 0$) deep centre with its $E_s = \frac{1}{2}E_s^c$, then the ratio of the thermal activation energy after and before lattice distortion is $E_b'/E_b = \frac{1}{4}[1 - 4E_s^c/(E_o - E_s^c)]^2$ and $[1 - 4E_s^c/(4E_o - E_s^c)]^2$, respectively [20]. Thus, strong luminescence observed from defect centres in nanocrystals is a natural consequence of the CIDSE. For the same reason, the band-edge relaxation also increases the capture cross-section of surface states, especially for those with their binding energy close to the conduction-band edge. Therefore, it is necessary to passivate the surface states for high efficiency from nanocrystals.

When a cubic crystal is strained anisotropically, its symmetry is lowered, and the crystal becomes birefringent. The [1 0 0] tensile strain resulting from excited electrons in the X valleys will dynamically change the crystal class from cubic to tetragonal. For tensile strain in the [1 1 1] direction caused by the excited electrons in the L valleys, the crystal will become trigonal. Both the tetragonal and trigonal crystal classes are optically uniaxial. Following the compressive uniaxial stress work given by [38, 39], it is straightforward to deduce the effects of tensile uniaxial stress on diamond and zinc-blend semiconductors. The Γ optical modes for Si and Ge are three-fold degenerate. For tensile stress parallel to either the [1 0 0] or [1 1 1] directions, the $k = 0$ optical phonons are split into a singlet, Ω_s, with its eigenvector parallel to the stress and a doublet, Ω_d, with their eigenvectors perpendicular to the stress. For these two stress directions, the singlet and doublet become

$$\begin{aligned} \Omega_s &= \omega_o - \Delta\Omega_H - \tfrac{2}{3}\Delta\Omega \\ \Omega_d &= \omega_o - \Delta\Omega_H + \tfrac{1}{3}\Delta\Omega \end{aligned} \tag{16}$$

where ω_o is the frequency of the $k = 0$ optical modes in the absence of strain; $\Delta\Omega_H$ represents the frequency shift due to the hydrostatic component of a tensile stress; and $\Delta\Omega = \Omega_s - \Omega_d = (-d\Delta\Omega/dF) \times F$ is the splitting of singlet and doublet modes under a tensile stress, F. In general, the tensile stress F is proportional to the strain energy $n(E_p - E_g)$. It is obvious from Equation 16 that for the tensile uniaxial stress case, the singlet mode parallel to the stress axis shifts to low energy monotonically with increasing tensile stress, while the shift of the doublet modes will depend on the competition of $-\Delta\Omega_H$ and $\frac{1}{3}\Delta\Omega$. The intensities of the singlet and doublet peaks are approximately in the ratio of 4:1, estimated from the first-order selection rules [39].

For III–V zinc-blend semiconductors, the Γ optical modes are still three-fold degenerate as analyzed by the symmetry selection rules. However, they are split by the long-range coulomb electric field induced by polar vibrational modes, into a singlet LO mode, with its wave vector parallel to the field, and doublet TO modes, with their wave vectors perpendicular to the field. The total polarization (ionic plus electronic) in the carrier-induced strained nanocrystals will automatically lie in the strain direction due to the relative displacements of the ions and electrons in the strain direction. Even for non-polar crystals, the uniaxial strain also can induce a polarization field in the strain direction due to transfer of bond charges [40–42]. Thus, the singlet mode propagating in the strain direction is, in fact, the LO mode, and the doublet modes are TO modes. Therefore, the TO(Γ) Raman peak for III–V nanocrystals cannot be further split by carrier-induced [0 0 1] and [1 1 1] tensile stress.

In addition, carrier-induced tensile strain will remarkably reduce the elastic constants, especially for those in the strain direction. Thus, almost all vibrational modes in nanocrystals will show a red shift with respect to the corresponding mode in their bulk. To our knowledge, there are no experimental data describing the red shift of vibrational modes with tensile stress for most semiconductors. It should be a valid approximation, in the elastic limit, to take the tensile stress rate of a vibrational mode as the same as that measured in the applied uniaxial stress case. Since the shear strain induced by excited free carriers dynamically breaks the lattice symmetry and relaxes the selection rules for crystal momentum conservation in Raman scattering, some vibrational modes with wave vector $k \neq 0$ will become Raman active in nanocrystals.

We can see from the arguments above that the one-electron energy band model is no longer a valid approximation for dealing with the optical transition in small nanocrystals, because the change in energy density caused by the electronic transition cannot be considered as a perturbation of the original crystal Hamiltonian. That is, the nanocrystals cannot be treated as a rigid cavity. The electronic transition is always accompanied by lattice relaxation due to the high energy density of nanocrystals. For this reason, the constraint of crystal momentum conservation on the optical transition is greatly relaxed in nanocrystal systems. The electronic wave functions in nanocrystals are the vibronic wave functions (the products of

electronic wave functions and vibrational wave functions), rather than the Bloch functions. Thus, the optical transitions in both direct- and indirect-gap nanocrystals show the multiphonon-assisted electronic transition processes in the configuration coordinate diagram (Fig. 1).

2. Experimental procedure

The highest priority on research and applications for nanocrystal materials is to produce the isolated, impurity controlled and monodispersed semiconductor nanocrystals. We have found that the powder processing of semiconductor materials can lead to extremely small nanocrystals with perfect lattice structure when size-selective dispersion techniques are applied. The nanocrystal samples used in this experiment were obtained by the size-selective precipitation method. In this method, ultrafine semiconductor powder is dispersed into ethyl alcohol to yield a suspension under vigorous stirring. Particle separation is based on sedimentation, either by gravity or by means of an ultracentrifuge. The final size distribution also depends on the solvents and solution concentrations. For a dilute particle solution in ethyl alcohol, a high monodispersion ($<5\%$ r.m.s.) can be achieved for the smaller size particle batch. The particle size was determined using a Hitachi H300 transmission electron microscope. A standard size deviation of about 10% was achieved for each particle batch. The obvious advantage of the powder processing of semiconductors is its ability to control the impurity and lattice structure of the nanocrystals rigorously, because the nanocrystals are synthesized from semiconductor wafers with known parameters.

The samples used in this study were obtained by drying the corresponding particle solutions on stainless steel sheets at room temperature. A microscope Raman system was employed for measurement of photoluminescence (PL) and Raman scattering. The exciting light was focused through a microscope optical system to a spot about 50 μm in diameter on the sample. The advantage of a microscope optical system is easy to obtain high excitation intensity. Photon-counting data for light analysed with a 0.85 m double-grating spectrometer. The spectral resolution of the measurement system is at least 0.2 meV.

The optical measurements under high pressure were performed in a gasket diamond-anvil cell using a 4:1 methanol:ethanol mixture or pure water as the pressure-transmitting medium. In order to obtain a strong signal for analysing, the samples with a high concentration of nanocrystals in the pressure-transmitting medium were used in this work.

3. Results and discussion

3.1. GaAs nanocrystals

The energy gaps at the Γ, L and X points in bulk GaAs electronic BZ are 1.52, 1.82 and 2.0 eV, respectively. The free exciton for the direct-gap in bulk GaAs has an effective diameter of about 20.8 nm, which si so large that GaAs nanocrystals are likely to show strong confinement effects. The quantum confinement will rapidly open up the direct energy gap of a GaAs nanocrystal with decreasing particle size. By using the effective-mass model and neglecting the interaction between the valleys, a simple estimate of the shift in the energy gaps with particle size indicates that the energy gap will become an indirect-gap with the X valleys as the lowest conduction-band edge when the particle size is reduced below 5.0 nm. The calculations, by means of a plane-wave pseudopotential method, also show that as the particle size is smaller than 3.0 nm, the band gap of GaAs nanocrystals will become an indirect gap with the X valley as its lowest band edge [22].

Fig. 2 shows the absorption spectra of GaAs nanocrystal colloids for three particle batches in which the particle size distributions are located at 10.0 ± 1 nm (sample 1), 4.0–5.0 nm (sample 2) and 3.0 nm (sample 3). The absorption spectrum for sample 1 exhibits a sharp direct-gap transition behaviour. The absorption spectra for both samples 2 and 3 show extensively broadened indirect-gap transition behaviour. The band gap, fitted by the relation $\alpha = A(E - E_g)^{1/2}$ is about 1.7 eV for sample 1. The band gap, estimated by the relation $\alpha = B(E - E_g)^2$, is about 2.2 and 2.5 eV for samples 2 and 3, respectively.

In Fig. 3 we show the Raman spectra for the three GaAs nanocrystal samples and the excitation behaviour of Raman scattering for samples 2 and 3. The LO(Γ) and TO(Γ) modes for bulk GaAs are 292.5 and

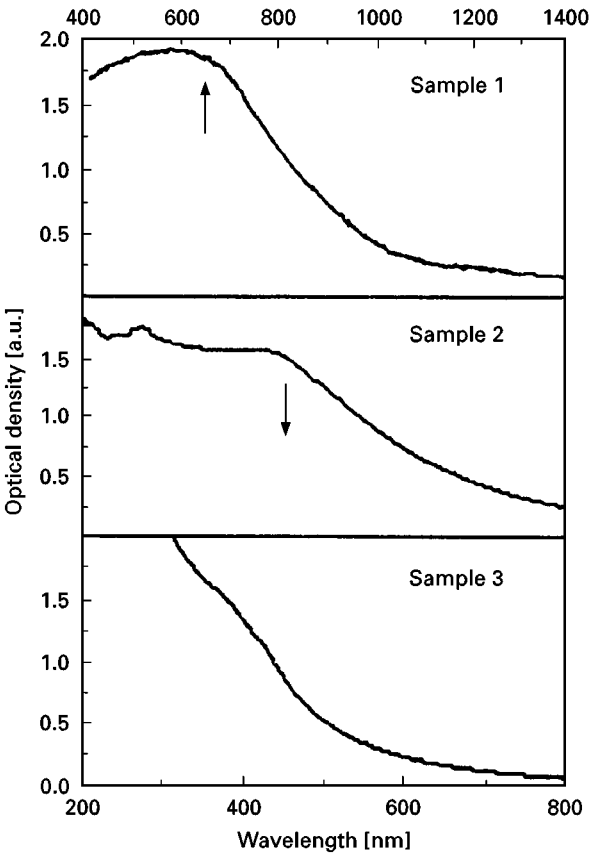

Figure 2 The absorption spectra for GaAs nanocrystal sample 1 with a particle size of 10 nm, sample 2 with a size of 4.0–5.0 nm and sample 3 with a size of 3.0 nm.

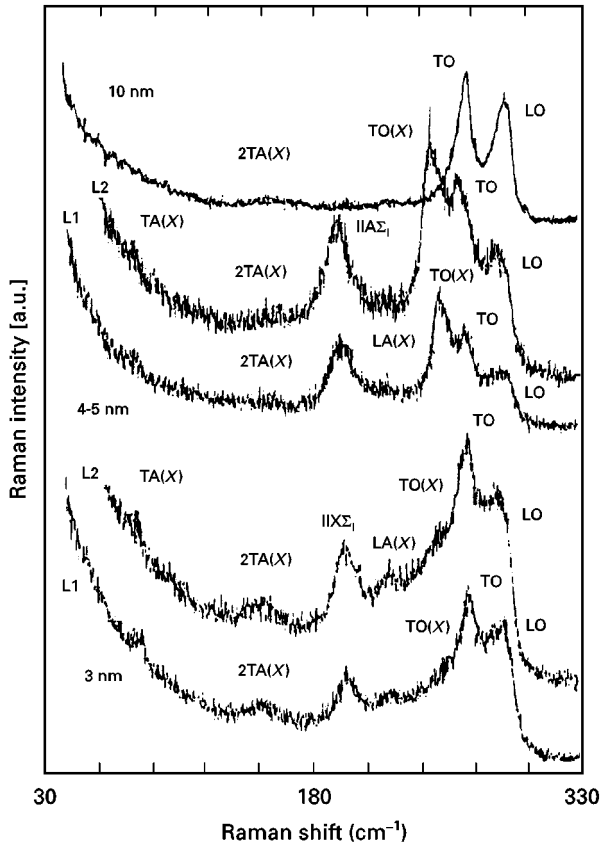

Figure 3 The Raman scattering spectra for GaAs nanocrystal samples 1–3. The excitation behaviour of Raman scattering for samples 2 and 3 is also shown in the figure. L1 and L2 represent the excitation intensity at 100 and 200 W cm^{-2}, respectively.

267.5 cm^{-1} (with a half-width of 3.1 cm^{-1}), respectively. The first-order Raman scattering of the large size GaAs nanocrystals in sample 1 only exhibits the LO and TO modes, as does the bulk GaAs. However, compared with the Raman spectrum of bulk GaAs, both the LO and TO peaks become broadened and red shifted. The half-width for both LO and TO peaks is about 20 cm^{-1}. The red shifts for LO and TO are 2.5 and 1.5 cm^{-1} at normal excitation

Both absorption and Raman spectra demonstrate that the large size GaAs nanocrystals retain direct bandgap and T_d symmetry. The excited free carriers in the Γ valley mainly produce pure dilational strain due to the S symmetry of the electronic wave function in the Γvalley [23, 26]. According to the carrier-induced dynamic strained quantum dot model, the red shifts for vibrational modes result from the tensile strain caused by excited free carriers. The red shift of vibrational modes should be $d\omega/dp \times \Delta P$, where $d\omega/dp$ represents the pressure rate of vibrational modes ($d\omega_{TO,LO}/dp = 0.43$ cm^{-1} kbar^{-1} for bulk GaAs), and $\Delta P = -(2\Delta E/KV)^{1/2}$, the carrier-induced stress. The carrier-induced stress in sample 1, estimated by the mean red shift of the LO and TO modes, is about 4.6 kbar. The stress ratio between two different size particles under the same excitation condition can be written as $\Delta P_1/\Delta P_2 = (V_2/V_1)^{1/2}$. If we assume that the volume ratio for the largest particle, V_1, and the smallest one, V_2 in sample 1 is 0.5, which corresponds to a particle size range of 8.0–12 nm, then the deviation of stress from its mean value is about ±70%, which corresponds to a stress deviation of ±3.3 kbar^{-1}. Thus, the inhomogeneity of particle size in the sample at most contributes 2.6 cm^{-1} to the half-width of the LO and TO Raman peaks. Similarly, broadened Raman peaks also have been observed in C_{60} fullerides, where the particle size is exactly the same [43]. Thus, inhomogeneity of particle size in nanocrystal samples is not important for explaining the broadened Raman spectrum observed in semiconductor nanocrystal systems, especially for the large sized nanocrystal sample.

The electron–phonon coupling in Raman scattering occurs in the intermediate states, which are not energy relaxation states. In principle, the electron–phonon coupling mechanism for Raman scattering in nanocrystals should be the same as in their bulk. However, any excitation on a nanocrystal unavoidably induces lattice strain due to the feature of high energy density, especially for the case where the photon energy is much higher than the band gap of the nanocrystals. Therefore, electron–phonon interactions in the intermediate states for Raman scattering no longer obey the constraint of crystal momentum conservation in nanocrystals. At a steady excitation, the carrier-induced volume change in sample 1 GaAs nanocrystals, estimated by the mean stress occurring in the sample, is about 0.06%. Since the large size GaAs nanocrystals retain T_d symmetry and direct bandgap, the carrier-induced strain is pure dilational, which can only be done by the anharmonic long-wavelength acoustical phonons with Γ symmetry, not by the Γ optical modes; because the Γ optical modes cannot displace the mass centre of unit cells and only the long-wavelength acoustical displacements can move all neighbouring unit cells by almost the same amount (dilational strain). In this case, an excited electron is not only scattered by the Γ optical phonons, but also has to emit or absorb such anharmonic acoustical phonons simultaneously in the intermediate states of Raman scattering. Thus, Raman scattering in large GaAs nanocrystals, in fact, is a multiphonon scattering process involving the Γ anharmonic acoustical phonons. The mean energy for such anharmonic acoustical phonons is about 1 m eV estimated in terms of the half-width of the LO and TO Raman peaks. This is just the acoustic phonon energy that an electron in a spherical symmetry valley of bulk GaAs can absorb (or emit), namely elastic scattering [26]. For this reason, the Raman scattering in direct-gap nanocrystals usually is broadened by the low energy anharmonic mode scattering, the degree to which depends upon the strain energy density created by excitation.

Fig. 4 depicts the PL spectra for the three GaAs nanocrystal samples at 77 K. The GaAs nanocrystal samples with the three different sizes are all made from the same GaAs wafer under the same condition. However, the largest size (10 nm) GaAs nanocrystals with direct-gap, even for those oxidized at 600 °C, do not show any PL at either 77 K or room temperature. The same behaviour for PL in this size range of GaAs nanocrystals has also been observed by other groups

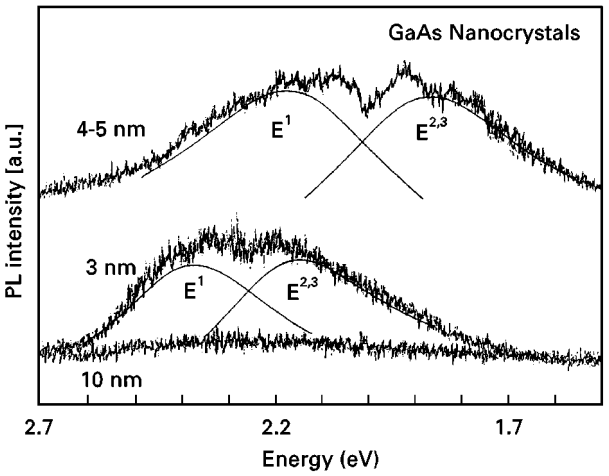

Figure 4 The PL spectra for GaAs nanocrystal samples 1–3 under excitation of the 457.9 nm line at 77 K. E^1 and $E^{2,3}$ represent the emission band from split higher energy states, E^1, and energy-relaxed band-edge states, $E^{2,3}$.

[44]. In contrast, the smaller size GaAs nanocrystals (without any passivation) with indirect-gap show fairly strong and broad PL. From the point of view of the CIDSE, it is not surprising for the largest size GaAs nanocrystals with direct-gap not to show any PL. As discussed previously, the electron–phonon coupling mechanism for excited electrons at the conduction-band edge is dominated by deformation potential coupling, which depends on the pressure rate (or stress rate) for the band gap and the strain energy density caused by excitation. The pressure rate for the Γ conduction-band edge of bulk GaAs is about 11 meV kbar^{-1}. Suppose the pressure rate of the band gap for the larger size GaAs nanocrystals remains the same as that for bulk GaAs, then the energy shift of the conduction-band edge for the larger size GaAs nanocrystals in sample 1, obtained by the mean stress (4.6 kbar), is about −50 meV. In order to maintain pure dilational strain, the energy relaxation of excited electrons at the Γ band edge must be achieved by emitting long-wavelength anharmonic acoustical phonons, which is about 1 meV as estimated by Raman scattering. In this case, the electron–phonon coupling strength calculated by $E_s^c = Sh\omega$ is about 50 for such anharmonic acoustical phonons. Thus, the 50 meV energy relaxation for the excited electrons at the Γ band edge will take a long time due to the cascade processes for emitting such acoustical phonons. This dramatically increases the radiative lifetime of the excited electrons at the Γ band edge. The intrinsic strong electron–anharmonic acoustical phonon coupling feature for the Γ band edge makes the large size direct-gap GaAs nanocrystals unable to show any PL. This intrinsic strong electron–anharmonic acoustic phonon interaction also explains the phase shift between current and voltage observed in large size GaAs nanocrystals [45]. For the same reason, we cannot expect to observe any measurable PL from the direct-gap InP nanocrystals [46]. However, most II–VI nanocrystals have uniaxial symmetry with wurtzite lattice structure. The energy relaxation of the excited electrons at the Γ conduction-band edge can be achieved by emitting relatively high energy acoustic phonons (from 101 cm^{-1} for ZnO to 43 cm^{-1} for CdS [41]), which has been observed in CdS nanocrystals [47]. In addition, the pressure rate of the direct band gap for II–VI nanocrystals is relatively smaller compared with that for III–V nanocrystals. Consequently, the radiative lifetime for the excited electrons at the Γ band edge of II–VI nanocrystals becomes relatively shorter than that for III–V direct-gap nanocrystals. Thus, the II–VI nanocrystals with wurtzite lattice structure can show weaker band-edge emission [15, 47].

In contrast to the direct-gap GaAs nanocrystals of sample 1, the small size GaAs nanocrystals in both samples 2 and 3 have indirect-gap with X valleys as their lowest conduction-band edge. The splitting of the X valleys of GaAs nanocrystals under a [1 0 0] strain is similar to that occurring in silicon nanocrystals, but has one longitudinal valley, E^1, up and two transverse valleys, $E^{2,3}$, down (Fig. 1). The value for the elastic compliance constant, $(S_{11} - S_{12})$, and the shear strain deformation potential, Ξ_u, in bulk GaAs are 1.54×10^{-12} dyn^{-1} cm^2 and 7.4 eV, respectively [26, 39]. The [1 0 0] tensile stress rate for the band-edge states, $E^{2,3}$, calculated by Equation 15, is −3.8 meV kbar^{-1}, which is much smaller than the pressure coefficient of the Γ valley. In addition, the shear uniaxial strain consists of differential displacements of the neighbouring unit cells, which can only be achieved by the short wavelength acoustical phonons required by the symmetry. The energy relaxation of the excited electrons in both the L and X valleys can be achieved by emitting such high energy acoustical phonons at the corresponding edge of the phonon BZ, which usually has a high density of vibrational states. Compared with the Γ valley, the excited electrons in both the L and X valleys have relatively shorter relaxation times. Therefore, the indirect-gap GaAs nanocrystals in samples 2 and 3 are able to show considerably strong band-edge emission at both 77 K and room temperature (Fig. 4).

The PL spectrum for GaAs nanocrystals in both samples 2 and 3 exhibits two emission bands that move to higher energy with decreasing particle size. Thus, the two emission bands in the PL spectrum must result from confined free electronic states. We identify that the higher energy band comes from the emission of the excited electrons at the unstable E^1 level, while the lower one results from the energy-relaxed band-edge states $E^{2,3}$, as shown in Fig. 4. By fitting the PL spectrum with Gaussian line shapes, the PL bands E^1 and $E^{2,3}$ for GaAs nanocrystals in sample 2 are located at 2.16 and 1.88 eV, respectively. The corresponding peaks for sample 3 are at 2.37 and 2.18 eV, respectively. The [1 0 0] tensile stress occurring in the GaAs nanocrystals of samples 2 and 3 is about 25 and 16 kbar, respectively, as obtained by the linear stress-splitting rate, $\Xi_u(S_{11} - S_{12})$. Therefore, the band gap and Stokes shift for GaAs nanocrystals in sample 2 (3) are about 2.1 (2.36 eV) and 0.187 (0.126 eV), respectively, which are roughly consistent with those measured by the absorption spectrum.

The energy of the TO(X) mode measured by neutron scattering is about 252 cm^{-1} [48]. The same mode measured by Raman scattering in sample 2 GaAs nanocrystals changes from 251 to 247 cm^{-1} with excitation intensity (Fig. 3). The $IIA\Sigma_1$ mode [similar to the LA(Σ) mode] measured by neutron scattering is about 198.7 cm^{-1} [48]. The same mode in small GaAs nanocrystals varies from 198 to 195 cm^{-1} (Fig. 3). According to the CIDSE, the Raman intensities for the vibrational modes with $k \neq 0$ should depend on the strength of the carrier-induced dynamic strain. Thus, the Raman intensities for the strain-sensitive modes TO(X) and $IIA\Sigma_1$ become much stronger in sample 2 than that in sample 3 (Fig. 3). The typical red shift for TA(X), TO(Γ) and LO(Γ) modes in sample 2 (sample 3) is 2 (1.5 cm^{-1}), 4 (2.5 cm^{-1}), and 7 (6 cm^{-1}), respectively (Fig. 3). Based on the stress obtained from the splitting of the PL spectrum, the tensile stress rate for TA(X), TO(Γ) and LO(Γ) is about -0.09, -0.16 and -0.28 cm^{-1} $kbar^{-1}$, respectively. The stress rate for the TO(Γ) mode measured in the applied uniaxial stress case is in the range 0.15–0.18 cm^{-1} $kbar^{-1}$ [39].

The LO and 2LO Raman intensities for GaAs nanocrystals in both samples 2 and 3 become much weaker compared with those observed in GaP nanocrystals (Fig. 5). The less efficiency of LO and 2LO Raman scattering in the small sized GaAs nanocrystals is perhaps caused by their band structure. Although the GaAs nanocrystals in samples 2 and 3 have X valleys as their lowest conduction-band edge, however, by the effective-mass model, the L valleys for Samples 2 and 3 GaAs nanocrystals lie only 0.3 and 0.5 eV higher in energy than that of the X band edge, respectively. In this case, the excited electrons may scatter between the L and X valleys. The electrons in the L valleys will induce the [1 1 1] dynamic strain [23]. Since the L valleys are not energy stable states, the small dynamic strain induced by the excited electrons in the L valleys will add a perturbation on the major [1 0 0] strain. As a result, the polarization field coupling with the LO mode will be decreased in the major [1 0 0] strain direction. Perhaps, this is the reason that small sized GaAs nanocrystals show less efficiency for both LO and 2LO Raman scattering.

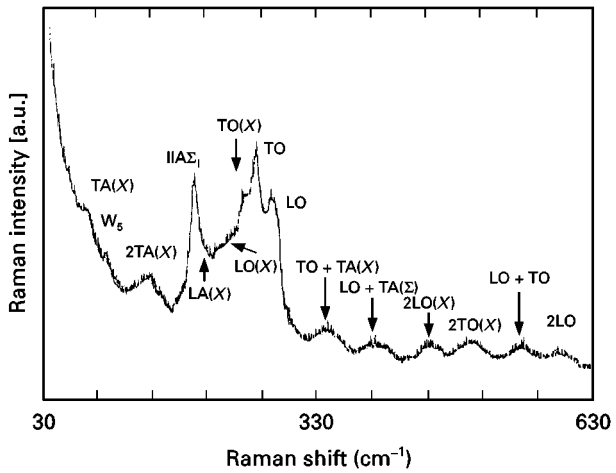

Figure 5 The first- and second-order Raman scattering spectrum for sample 3 GaAs nanocrystals under excitation of the 488 nm line.

Since the red shift of vibrational modes depends on the tensile stress, which is proportional to the strain energy, $n(E_p - E_g)$, here n is the density of excited electron–hole pairs, if photon energy and excitation intensity are kept constant, then the vibrational modes of the GaAs nanocrystals in sample 3 should show a relatively smaller red shift than that in sample 2 due to the large band gap of GaAs nanocrystals in sample 3. This is exactly the Raman behaviour we have observed in the small sized GaAs nanocrystals, as shown in Fig. 3. In Fig. 3 we also show the dependence of vibrational modes of GaAs nanocrystals in samples 2 and 3 on excitation intensity. When the excitation intensity is increased from level 1 (100 W cm^{-2}, by the 488 nm line) to level (200 W cm^{-2}), the red shifts of the LO, TO, TO(X), and $IIA\Sigma_1$ vibrational modes of GaAs nanocrystals in Sample 2 are 4.5, 2, 3 and 2 cm^{-1}, respectively. However, the same vibrational modes in the GaAs nanocrystals of sample 3 all show a small red shift of less than 1 cm^{-1} at the same excitation condition. In fact, it is a natural consequence of the CIDSE that at the same excitation condition, the vibrational modes in smaller size particles show relatively smaller red shifts and broadening than that in larger sized particles. A more detailed discussion about this feature will be given in the section on silicon nanocrystals and porous silicon.

3.2. GaP nanocrystals

In Fig. 6a, b we show the first- and second-order Raman spectra for bulk GaP and GaP nanocrystals with a mean size of 4.0 nm. The Raman peaks were identified in the figures in terms of phonon energy and symmetry. Peak B (34.7 meV), which occurred in both bulk GaP and nanocrystals was identified in lecture to be electronic Raman scattering by the neutral acceptor Mg, dissolved in the Ga sites in GaP [49]. Compared with Raman scattering in bulk GaP, all vibrational modes in GaP nanocrystals become soft, and the degree to which depends on excitation intensity. The typical red shifts of the TA(X), TO(Γ) and LO(Γ) modes in GaP nanocrystals with respect to those in bulk GaP are 1, 1.5 and 5 cm^{-1}, at normal excitation by 457.9 nm line (Fig. 6a). Another remarkable feature of the Raman scattering in GaP nanocrystals is that the Raman intensity of the LO(Γ) and 2LO(Γ) peaks becomes much stronger than that in the corresponding bulk GaP. The enhanced Raman intensity of the LO(Γ) and 2LO(Γ) peaks doe not reflect that Fröelich coupling [the interaction of an excited electron with the long-range electric field induced by the LO(Γ) mode] is increased in GaP nanocrystal. As discussed above, the excited electrons in the X valleys will produce a shear strain in the [1 0 0] direction by emitting high energy acoustical phonons. The shear strain must lead to relative displacements of metallic (Ga) ions with respect to the non-metallic ions (P) in the strain direction. These internal displacements will create a polarization field, which will enhance the long-range electric field induced by the LO mode.

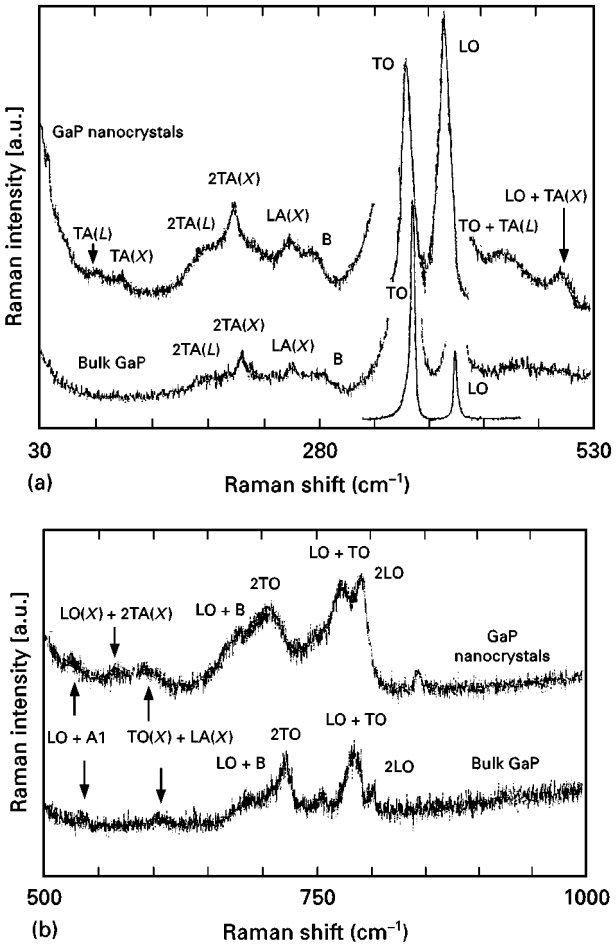

Figure 6 (a) and (b) show the first- and second-order Raman scattering spectra for GaP nanocrystals with a size of 4.0 nm and bulk GaP. Compared with bulk GaP, the intensity ratio for the TO (2TO) and LO (2LO) Raman peaks becomes reversed in GaP nanocrystals.

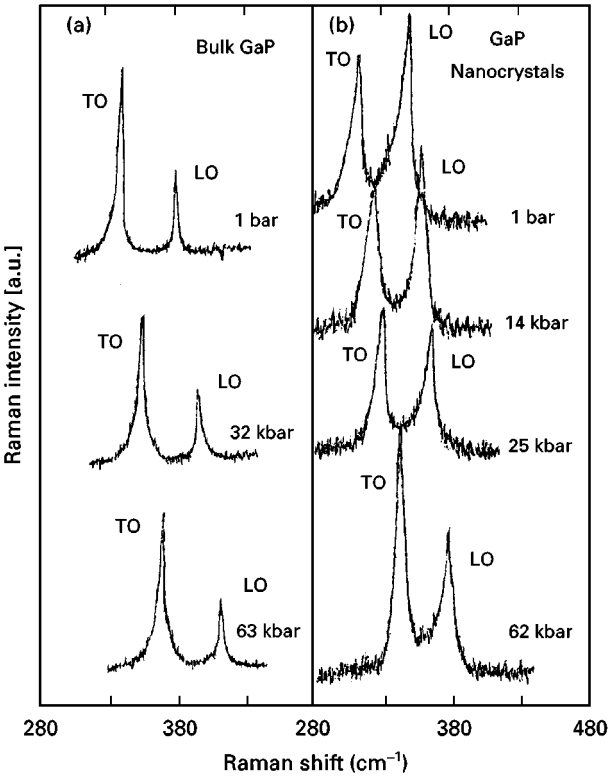

Figure 7 (a) and (b) depict the pressure behaviour of the TO and LO Raman intensity in bulk and GaP nanocrystals, respectively.

Thus, the enhanced Raman intensity for LO(Γ) and 2LO(Γ) observed in the GaP nanocrystal may result from piezoelectric coupling caused by the carrier-induced uniaxial strain [50].

In order to further prove the piezoelectric effect caused by excited free carriers in indirect-gap GaP nanocrystals, Raman scattering for bulk GaP and nanocrystals with a size of 4.0 nm was performed under hydrostatic pressure. Fig. 7a, b depicts the typical Raman spectra for GaP nanocrystals and the corresponding bulk GaP at several pressures. The Raman intensity of the TO modes in bulk GaP remains higher than that of the LO mode over the entire measured pressure range (1 bar to 60 kbar), and the relative intensity of the TO and LO mode basically remains the same. A similar result has been observed by others [51]. The pressure rate of the TO and LO modes for bulk GaP is 0.45 and 0.43 $cm^{-1}\,kbar^{-1}$, respectively. However, the Raman intensity of the LO mode in GaP nanocrystals becomes much higher than that of the TO modes at atmospheric pressure. With increasing pressure, the Raman intensity of the LO and 2LO Raman peaks rapidly decreases, and, at about 60 kbar, the intensity ratio of the TO and LO Raman peaks in GaP nanocrystals reaches the same as that in bulk GaP, while the pressure rate for the LO and TO modes in GaP nanocrystals becomes 0.45 and 0.43 $cm^{-1}\,kbar^{-1}$, respectively. In addition, the half-width of the LO and TO Raman peaks decreases and first-order Raman scattering for all vibrational modes with $k \neq 0$ disappears with increasing pressure.

According to the definition of piezoelectric polarization, the electron–LO phonon coupling strength, through the polarization generated by the piezoelectric effect, is proportional to shear strain [50]. Since an applied pressure can effectively constrain the shear strain induced by excited free carriers, thus the polarization field induced by the shear strain decreases with increasing pressure. Consequently, the Raman intensity of the LO phonon in GaP nanocrystals shows a relatively fast decrease compared with that in bulk GaP. When the applied pressure is strong enough to constrain the tensile strain caused by excitation, first-order Raman scattering for the vibrational modes with $k \neq 0$ becomes forbidden, because Raman scattering in a rigid nanocrystal must obey the selection rule of crystal momentum conservation.

Fig. 8 shows the PL spectra of GaP nanocrystals at several pressures. The PL spectrum of GaP nanocrystals with size of 4.0 nm exhibits three peaks. By fitting the PL spectrum with Gaussian line shapes, the peaks are located at 2.45, 2.23 and 1.85 eV. According to their energy and pressure behaviour, we attribute the two higher energy peaks to emission from the splitting levels, E^1 and $E^{2,3}$, respectively, and the lowest one to emission from defect states, E_d. The corresponding defect emission band in bulk GaP was also shown in Fig. 8. It is clearly seen from Fig. 8 that, at first, the E^1 peak moves to lowest energy with increasing pressure at a rate of about -3 ± 0.5 meV $kbar^{-1}$, while the

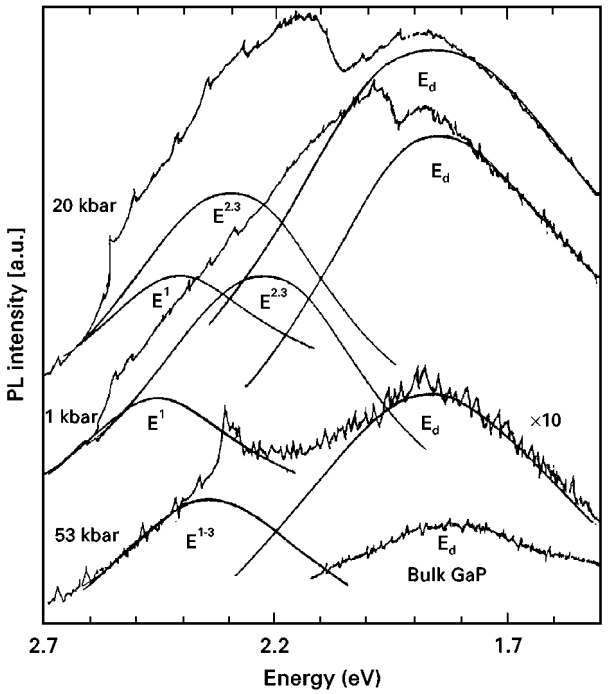

Figure 8 The PL spectra of GaP nanocrystals at several pressures. E^1 and $E^{2,3}$ represent emission bands resulting from splitting E^1 and $E^{2,3}$ band states, E_d depicts the emission band from defect states. The corresponding defect emission band in bulk GaP is also shown in the figure.

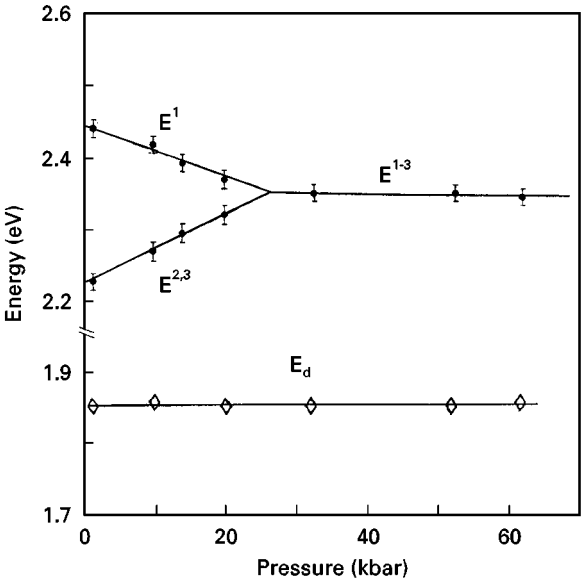

Figure 9 The pressure dependence of the emission bands E^1, $E^{2,3}$ and E_d measured in GaP nanocrystals with a size of 4.0 nm under excitation of a 457.9 nm line.

band-edge emission peak, $E^{2,3}$, moves to higher energy at a rate of 5.4 ± 0.2 meV kbar^{-1} (Fig. 9). When the pressure is over 27 kbar, the PL intensities from both confined electronic states and defect states become ten times lower than that at atmospheric pressure. At the high pressure range, a sharp structure, which may result from surface states, occurs at the energy of the band-edge emission as shown in Fig. 8. The energy of this new peak basically does not change with pressure. For this reason, the pressure rate of the band-edge emission for this nanocrystal sample cannot be measured at the higher pressure range. The lowest emission band, E_d, resulting from unknown deep levels is also independent of pressure in the pressure range measured in this work (Fig. 9).

The pressure dependence of the PL and Raman scattering of GaP nanocrystals provides an important test of CIDSE. As discussed previously, the carrier-induced strain in the [1 0 0] direction will split the three-fold degenerate X valleys of a GaP nanocrystal into one up, with a stress rate $\frac{2}{3}(S_{11} - S_{12})\Xi_u$, and the two down, with a stress rate $-\frac{1}{3}(S_{11} - S_{12})\Xi_u$. The strain compliance constant, $(S_{11} - S_{12})$, and the deformation potential constant, Ξ_u, are 1.25×10^{-12} dyn^{-1} cm^2 and 6.2 eV for bulk GaP, respectively [26, 39]. Since the applied hydrostatic pressure can effectively constrain the strain induced by excited free carriers, it can be seen from Fig. 1 that at the low pressure range, the emission peak, $E^{2,3}$, from the band edge should move to higher energy with a pressure rate $2 \times \frac{2}{3}(S_{11} - S_{12})\Xi_u$, and the higher energy peak, E^1, should shift to lower energy with a pressure rate $-\frac{1}{3}(S_{11} - S_{12})\Xi_u$, because the energy relaxation of the valence band decreases with a pressure rate $-\frac{1}{3}(S_{11} - S_{12})\Xi_u$. The pressure rates calculated by using this equation and the constants above are about -2.8 and 5.2 meV kbar^{-1}, which are in good agreement with the experimental results. From the cross-over pressure (27 kbar given by Fig. 9), we find that the Stokes shift is about 0.14 V and the band gap for GaP nanocrystals of 4.0 nm in size is about 2.37 eV, which is a little smaller than that predicted by the effective-mass model. When the applied pressure is over 27 kbar, the band-edge relaxation induced by excitation is completely constrained by the applied pressure. As this happens, the PL intensities from both band-edge emission and defect emission become much weaker for indirect-gap GaP nanocrystals. The optical transition in GaP nanocrystals changes from a multi-phonon-assisted electronic transition to one controlled by crystal momentum conservation. In this case, the nanocrystals with indirect-gap will return back to being a poor band-edge emission material, as is their bulk crystal.

The pressure dependence of the capture cross-section for a deep centre directly relies on the pressure dependence of the barrier energy, E_b. Because applied pressure reduces the lattice constant and constraints the energy relaxation for both band edge and deep centres, it is obviously seen from Fig. 1 that the barrier energy for a deep centre in direct-gap nanocrystals will monotonically increase with increasing pressure. In general, the emission intensity from deep centres decreases with increasing pressure, as observed in bulk GaAs and CdS nanocrystals [15, 35]. Compared with direct-gap nanocrystals, the capture cross-section for most deep centres in indirect-gap nanocrystals will reduce slowly, as is the case observed in GaP nanocrystals, since the down shift of the conduction-band edge caused by pressure may decrease E_b. The pressure results of the PL from confined electronic states and defect states in GaP nanocrystals further prove

the consistency and validity of the carrier-induced dynamic strained quantum dot model.

3.3. Silicon nanocrystals and porous silicon

As discussed in Section 1.1, excited electrons at the conduction-band edge of a silicon nanocrystal will induce [1 0 0] direction strain, which, in turn, splits the six-fold degenerate valleys into two up (transverse) and four down (longitudinal). In the meantime, the three-fold optical modes are split into a low energy singlet LO mode, with it's wave vector parallel to the strain direction and high energy doublet TO modes, with their wave vectors perpendicular to the strain direction. Compared to GaAs and GaP, silicon has a relatively narrow band gap and weak confined effect (with a Bohr radii of 4.3 nm). As shown previously, the photon energy required to excite one electron–hole pair at an equilibrium state should be $\frac{3}{2}E_g$, and $\frac{1}{2}E_g$ energy of the photon is to be used to produce lattice strain. In order to show the carrier-induced strain effect, strong excitation experiments under the 488 nm line from an Ar^+ laser were performed on different size silicon nanocrystals. The excitation intensity was varied from 500 to 2000 W cm^{-2} in increments of 500 W cm^{-2} (from levels 1–4) and the illuminated area was maintained the same as the excitation intensity was changed.

In Figs 10 and 11a we show the excitation behaviour of PL and Raman scattering for large size (10 ± 1 nm) silicon nanocrystals. The confined energy for this size Si particles is about 0.1 eV, as estimated by the effective-mass model. As the excitation intensity increases, the Raman spectrum for the three-fold degenerate optical modes broadens and splits into a lower energy, LO, mode and higher energy doublet, TO, modes. For large size particles, the doublet TO modes basically retain the same energy as that of the Γ optical modes measured at low excitation. In principle, the doublet TO modes should have a red shift, because any uniaxial strain always have a pure dilational component, which will move the weight centre

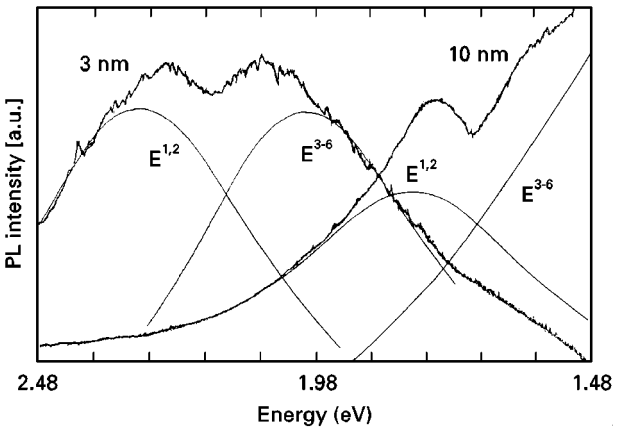

Figure 10 The PL spectra for the larger (10 nm) and smaller (3 nm) size Si nanocrystals at the excitation intensity of levels 4 and 3, respectively. $E^{1,2}$ and E^{3-6} show the emission bands resulting from split high lying $E^{1,2}$ levels and band-edge states E^{3-6}, respectively. The peak of the E^{3-6} emission band for 10 nm Si nanocrystals is located at 0.8 eV.

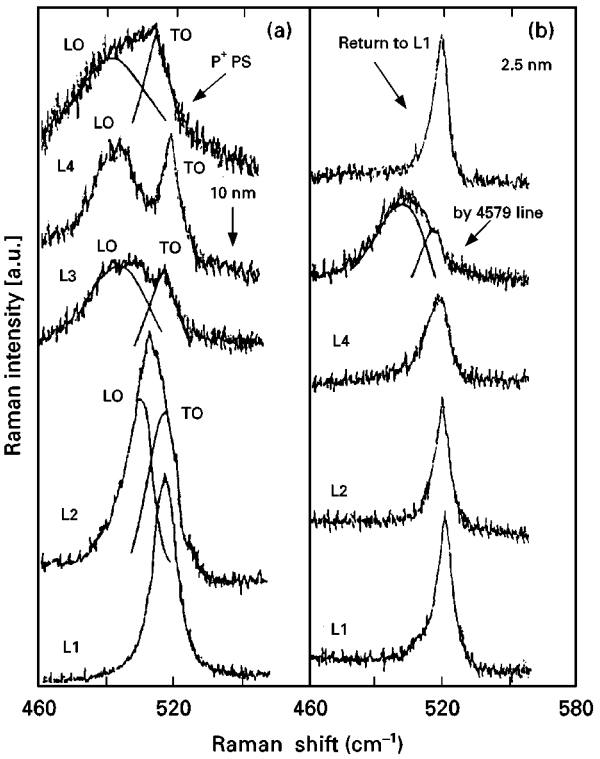

Figure 11 (a) and (b) show the excitation behaviour of the Γ optical modes in larger and smaller size Si nanocrystals, respectively. The Raman spectrum for a p^+ porous Si under excitation level 1 is also shown in (a). The Raman spectrum for the same smaller size Si nanocrystals under excitation of the 457.9 nm at excitation level 3 is given in (b).

of Γ optical modes to lower energy (Equation 16). However, a pure shear strain involving a uniaxial stretch along the [1 0 0] major axis must be accompanied by a symmetrical compressive strain perpendicular to the stretch direction, which will enhance the energy of the doublet TO modes. The Raman intensities of the LO and TO modes observed in large silicon nanocrystals are approximately in the ratio of 4:1, which is in good agreement with the result expected from the selection rules for first-order Raman scattering [39]. The sharp LO and TO modes split by excitation further demonstrate that in a carrier-induced optical uniaxial system, the splitting LO mode automatically lies on the strain axis and is independent of the direction of light passing through the nanocrystals [41, 52]. All these facts consistently support the identification of the splitting modes occurring in Si nanocrystals. The experimental datum for such splitting under an applied stress along the [0 0 1] and [1 1 1] directions in bulk Si is about 0.15 and 0.23 cm^{-1} kbar^{-1}, respectively [38]. However, the experimental datum for the compressive case was obtained for incident light perpendicular to the stress. In order to be consistent with stress splitting of the band-edge states of Si nanocrystals, we take the stress rate for LO–TO splittings as 0.2 cm^{-1} kbar^{-1} in the tensile strain case.

The Si nanocrystals, with a size around 10 nm, do not show any PL at excitation level 1. As the excitation intensity increases, the Raman spectrum for Γ optical modes becomes red shift and broadening,

which reflects that carrier-induced dynamic strain in the nanocrystals is enhanced with increasing excitation intensity. Consequently, the constraint of crystal momentum conservation for optical transition in the bulk is relaxed and the optical transitions in the dynamic strained Si nanocrystals become a multi-phonon-assisted electronic transition process. At excitation level 4, the LO–TO splitting observed on the Raman spectrum is 22 cm^{-1}, which corresponds to a 110 kbar stress occurring in the excited nanocrystals. At the same excitation, the strong PL spectrum of the same Si nanocrystals shows a sharp peak at 1.75 eV and another strong and broad emission band at 0.8 eV as measured by a PbS detector. By using a Gaussian line-shape to fit the PL spectrum, the higher energy emission band is located at 1.8 eV with a half-width of about 0.3 eV. Linear splitting of levels $E^{1,2}$ and E^{3-6} under a tensile uniaxial stress, F, follows $E^{1,2} - E^{3-6} = F \times \Xi \times (S_1 - S_2)$, where the shear deformation potential constant, Ξ_u, is 9.2 eV, and the elastic compliance constant, $(S_{11} - S_{12})$, is 0.982×10^{-12} dyn cm^2 for bulk silicon [26, 39]. Thus, the splitting of $E^{1,2}$ and E^{3-6} at excitation level 4 should be 0.99 eV. This splitting, measured by the PL spectrum, is 0.95 eV, which is basically consistent with the value estimated by the linear splitting, above.

As the silicon nanocrystals are made smaller, the two splitting peaks, $E^{1,2}$ and E^{3-6}, move into the measurement region, as shown by the PL of silicon nanocrystals with a size of 3.0 nm in Fig. 10. The higher energy $E^{1,2}$ peak and low energy E^{3-6} peak, obtained in terms of the Gaussian-line shape fitting technique, are located at 2.3 and 2.0 eV, respectively. Two similar emission bands of Si nanocrystals have been observed by others [53]. The Raman spectrum for the same Si nanocrystals is shown in Fig. 12 at the same excitation intensity. The stress occurring in the nanocrystals is about 35 kbar, as measured by splitting of the LO and TO modes. The splitting of $E^{1,2}$ and E^{3-6} levels, calculated by the linear splitting, is 0.315 eV, which is in good agreement with the value measured by the PL spectrum. From the carrier-induced stress, F, and taking into account the energy relaxation of the valence band edge, the Stokes shift should be $\frac{2}{3} F \times \Xi \times (S_{11} - S_{12})$, (see Fig. 1). Thus, in the absence of strain, the weight centre for the six-fold-degenerate conduction band is located at about 2.18 eV, which is close to the value predicted by the effective-mass model [5].

When the particle size distribution in the sample is relatively broad, the structure-splitting spectrum will not be so sharp, as shown in Fig. 10. Fig. 13 depicts the excitation behaviour of the PL spectrum for the silicon nanocrystals with a size of 4.0–5.0 nm. The corresponding Raman spectrum is similar to that observed for 3.0 nm Si nanocrystals, except for a little broadening (Fig. 12). As excitation intensity increases, the half-width of the PL spectrum is increased due to the enhanced splitting of levels $E^{1,2}$ and E^{3-6} caused by excitation. At the same time, the weight centre of the PL moves to higher energy due to increase of the electron population in the higher splitting level, $E^{1,2}$.

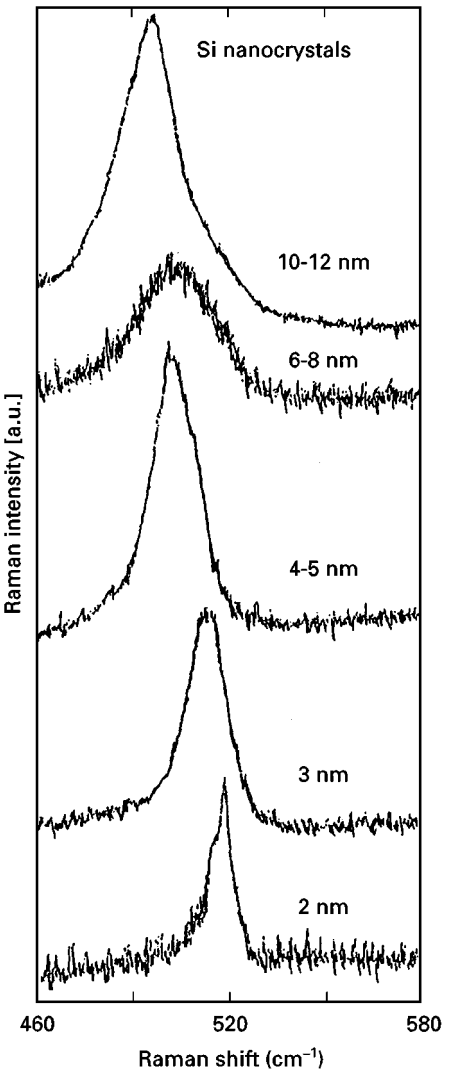

Figure 12 The size dependence of the Raman spectra of silicon nanocrystals under the excitation intensity of level 3. The red shift and broadening of the Raman spectra for the Γ optical modes increase with increasing particle size.

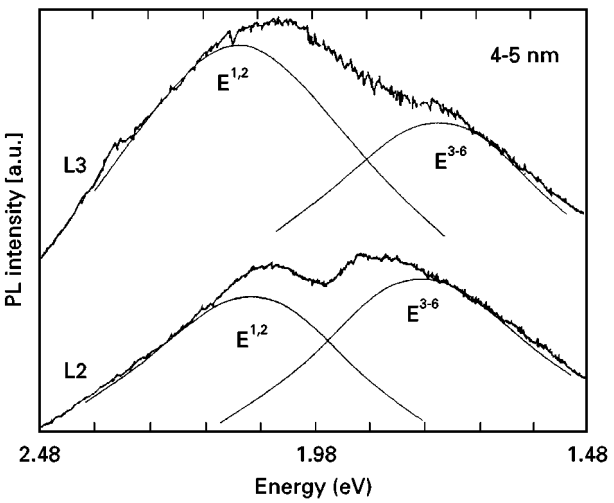

Figure 13 The excitation behaviour of the PL spectra for Si nanocrystals with a size of 4.0–5.0 nm at excitation intensity levels 2 and 3 under the 488 nm line. $E^{1,2}$ and E^{3-6} represent the emission bands resulting from the split high lying unstable $E^{1,2}$ levels and the band-edge, E^{3-6}, respectively.

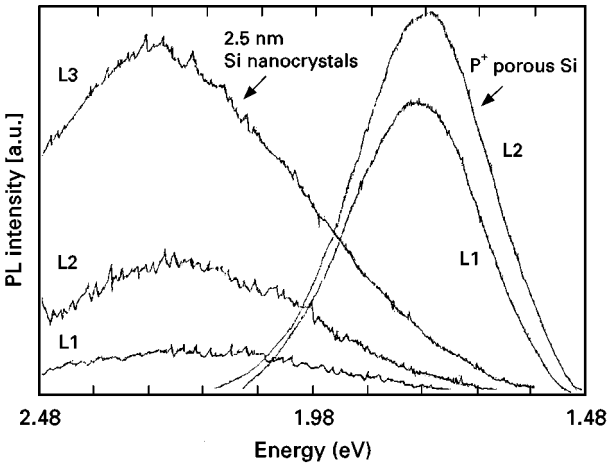

Figure 14 The excitation behaviour of the PL spectra for the Si nanocrystals with a size in 2.5 nm and a p^+ porous Si sample under different excitation intensities (from levels 1 to 3).

In Figs 11b and Fig. 14 we show the excitation behaviour of the Raman and PL spectra for small silicon nanocrystals with a size of 2.5 nm. In Fig. 14 we also show the excitation behavior for a p^+ porous silicon sample. At excitation level 1, the Raman spectrum for the Γ optical modes shows a peak at 520 cm^{-1}, while the weak PL spectrum has a peak at around 2.15 eV. With increasing excitation intensity, the Raman peak shows a relatively smaller red shift and broadening compared with that in the large size particles at the same excitation intensity. Simultaneously, the PL spectrum is rapidly enhanced and broadened. The excitation behaviour of the PL for smaller Si nanocrystals also shows that there still exists constraint of crystal momentum conservation for optical transitions even in small size indirect-gap nanocrystals. The strong luminescence can be achieved only when the dynamic strain induced by excited carriers is strong enough to relax the selection rule of crystal momentum conservation. That is, strong light emission in indirect-gap nanocrystals must be accompanied by broadening and red shift of the Raman spectra.

However, when the excitation light was changed from the 488 nm line to the 4579 nm line, the excitation behaviour of Raman scattering for smaller Si nanocrystals becomes quite similar to that observed in the larger particles, as shown in Fig. 11b. The reason is clear. As discussed in the section for GaAs nanocrystals, the red shift and broadening of the Raman peak directly depends on carrier-induced strain, which is dominated by the increase in strain energy of a nanocrystal. The strain energy induced by excitation is proportional to $n(E_p - E_g)$, where n is the density of excited electron–hole pairs in a nanocrystal and E_p is the photon energy. Since the energy gap, E_g, for nanocrystals is rapidly increased by quantum confinement, thus at the same excitation condition, the strain energy density occurring in a nanocrystal will decrease with decreasing particle size. Fig. 12 depicts typical Raman spectra of Si nanocrystals for several size ranges at the same excitation condition. We can clearly see that the red shift and broadening of Raman spectra increase with increasing particle size (in the nanometre size range).

The Raman scattering results obtained on GaAs, GaP and Si nanocrystals are naturally consistent with the carrier-induced dynamic strained quantum dot model. We can conclude that the red shift and broadening of vibrational modes in nanocrystals are dominated by the strain energy density caused by excited free carriers, not by phonon confinement. The experimental results obtained in this work are in sharp contrast to the prediction of the phonon confinement model. In addition, the phonon confinement model cannot explain why the acoustical modes and the optical modes at the edge of the photon BZ all exhibit a red shift, and why the red shift changes with photon energy and excitation intensity in nanocrystal systems. The experimental evidence for the phonon confinement model originated from the red shift and broadening of the Γ Raman peak observed from large size Si crystallites in glasses and amorphous silicon [19, 54]. Then the phonon confinement concept was settled on the basis of phonon uncertainty. From the dependence of the red shift of Γ Raman modes upon nanocrystal size and excitation intensity obtained in this work, it is clear that the experimental foundation for the photon confinement model is not solid. In addition, all the physical concepts have to be consistent with the entire structure of physics. The basic nature of the phonon is mechanical vibration of a lattice at its equilibrium position. Does phonon uncertainty have so strong an effect on the energy of the Γ optical mode, which remains its mass centre static? Thus, the nature of phonon confinement may need to be reconsidered in principle.

A question which we have to address is the temperature effect associated with the excitation. Under an excitation, the strain energy occurring in a nanocrystal is proportional to $n(E_p - E_g)$. Suppose the density, n, of the excited electron–hole pair is 10^{21} cm^{-3}, and $(E_p - E_g)$ is 1 eV. Then the stress occurring in a Si nanocrystal, calculated from Equation 14, is about 56 kbar, which will induce a down shift of 11.2 cm^{-1} for the LO(Γ) mode. We further assume that all strain energy is transferred into thermal energy. For this example, the increase of lattice temperature in the Si nanocrystal is about 97 K, calculated by $n(E_p - E_g)/c_p$, where c_p is the heat capacity at constant pressure (c_p is 1.65 $J\,K^{-1}\,cm^{-3}$ for Si). According to the temperature dependence of the Γ optical modes measured for crystalline Si [55], the red shift of the Γ optical modes caused by the increase in temperature is, at most, 1.8 cm^{-1}, which is much smaller compared with the corresponding red shift induced by carrier-induced stress. In addition, the strong excitation is somehow similar to laser annealing, which can eliminate the uniaxial strain induced by excited free carriers. Fig. 15 depicts the excitation behaviour of the Γ optical modes in 15–20 nm Si nanocrystals. When the excitation intensity is higher than level 4, instead of a red shift, the Raman peak of the Γ optical modes moves back to higher energy. This fact further shows that below excitation level 5, the red shift and broadening of the Raman spectra of vibrational modes are

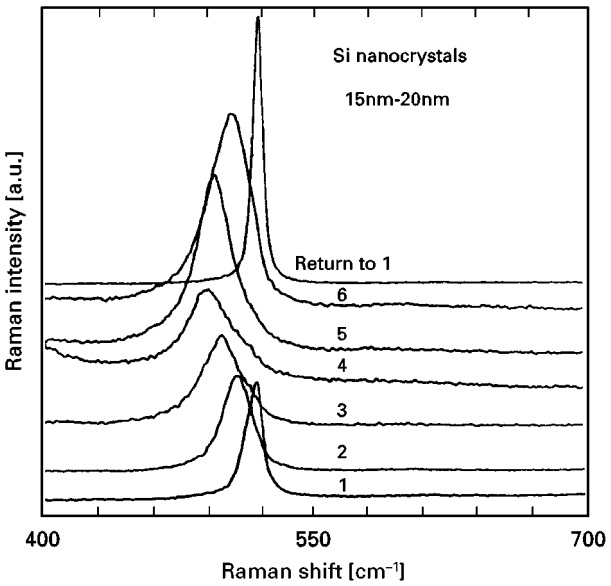

Figure 15 The excitation behaviour of the optical modes for the large Si nanocrystals with a size of 15–20 nm. As the excitation intensity is higher than level 4, the Raman peak, instead of being red shifted, moves back to higher energy due to the laser annealing effect.

dominated by carrier-induced strain effects. When the excitation intensity returns to level 1 after high excitation, the Raman spectra for both small and large Si nanocrystals essentially remain the same as before. Thus, carrier-induced strain is elastic, even when the uniaxial stress is more than 110 kbar.

Compared to the excitation behaviour of small Si nanocrystals (Fig. 14), the p^+ porous silicon sample shows a smaller red shift and less broadening as excitation intensity varies from level 1 to 4. The Raman spectrum for the same porous silicon sample shows a splitting of about 25 cm^{-1} between the LO and TO modes at excitation level 1. The corresponding stress occurring in the sample is about 125 kbar, similar to that observed in larger sized Si particles (Fig. 11a). The splitting of $E^{1,2}$ nd E^{3-6} at this stress is 1.13 eV, as obtained by linear splitting. Thus, the PL observed from the porous silicon sample, in fact, results from the lowest four-fold degenerate E^{3-6} levels, which have an energy relaxation of about 0.38 eV, as obtained by Equation 15. Taking into account the energy relaxation occurring in the valence band, the band gap for this porous silicon sample is about 2.5 eV, which is quite close to that of silicon nanocrystals with a size of 2.5 nm. (Fig. 14). We can see from Fig. 11b that Raman broadening induced by the same excitation condition is only about 5 cm^{-1} in this size silicon nanocrystals. Thus, there exists at least 20 cm^{-1} (corresponding to 100 kbar uniaxial stress) splitting between the LO and TO modes resulting from the static uniaxial strain residing in the silicon particles of porous silicon. The static strain resident in porous silicon has been observed by a number of groups in terms of X-ray diffraction technique [56]. The tensile strain occurring in porous silicon was found to increase with formation current density and intensity of illumination [57].

However, there has been no acceptable model of the formation mechanism of porous silicon that can explain why the anodic dissolution process of crystalline Si forced by an electric current can induce such a large residual strain in nanometre Si particles. On the basis of the carrier-induced strain model, we have proposed that when the current density for the anodic etching process is fixed, the carrier-density passing through the tip of a pore is greatly increased as the porosity of the etched layer increases. When the tip of a pore comes into the nanometre range, the stress occurring in a narrow tip is close to $\frac{2}{3}(nE_g/K)^{1/2}$. Suppose E_g in the nanometre sized tip is 1.5–2.0 eV, due to quantum confinement, and the carrier density is about 10^{20}–10^{21} cm^{-3}. The stress in the narrow tip could reach from several tens to hundreds of kilobars. Under the large strain occurring in a narrow tip, the anodic process will grow a SiH_x compound on the tip surface, which, in turn, fixes a strain on the lattice of the tips by lattice mismatch between the silicon and the surface layer. When the stress in the tip is strong enough to crack the tip, then the anodic dissolution process stops and the passivated and uniaxial strained nanometre size Si particles are left in the etched layer [21]. Thus, porous Si usually exhibits optic uniaxial properties, as has been observed by other groups [33].

Unlike silicon nanocrystals, the energy levels $E^{1,2}$ and E^{3-6} in porous silicon are separated by a static residual strain, which varies with anodic conditions. Therefore, it is quite reasonable to identify that the blue-fast emission band observed in porous silicon results from energy unstable $E^{1,2}$ states, while the red-slow emission band comes from the energy-relaxed band-edge states, E^{3-6} [58].

The pressure behaviour of the PL and Raman scattering for the porous silicon sample can further identify that the optical properties of porous silicon are dominated by strained silicon quantum dots. The precipitation for the porous silicon samples was reported in [21]. Here we need to point out some attention to the optical measurement under hydrostatic pressure. Because the optical properties of nanocrystal systems are dominated by the carrier-induced strain effect, it becomes critically important to maintain a constant excitation intensity while the pressure is being changed. Otherwise, the experimental data under pressure have no strictly physical meaning. In addition, the weak Raman signal of porous silicon cannot be measured by the normal back scattering geometry used in high-pressure Raman scattering. We used a diamond-anvil cell with a 45° incident light path, and the resulting Raman signal was collected by a microscopic objective at right angles to the sample surface. Compared to the back scattering system, the present system has higher collection efficiency and a higher signal-to-noise ratio [15].

Fig. 16 shows the PL spectra of p^+ porous silicon at several pressures. The PL peak energies at 1 bar for p^+ porous Si is 1.74 eV. In Fig. 17 we show the pressure dependence of the PL peak energy of both p^+ and p^- porous Si samples. For the p^+ (p^-) sample, the PL peak energy shifts to higher energy with increasing pressure at the rate of 6.2 (6.5) meV $kbar^{-1}$ up to

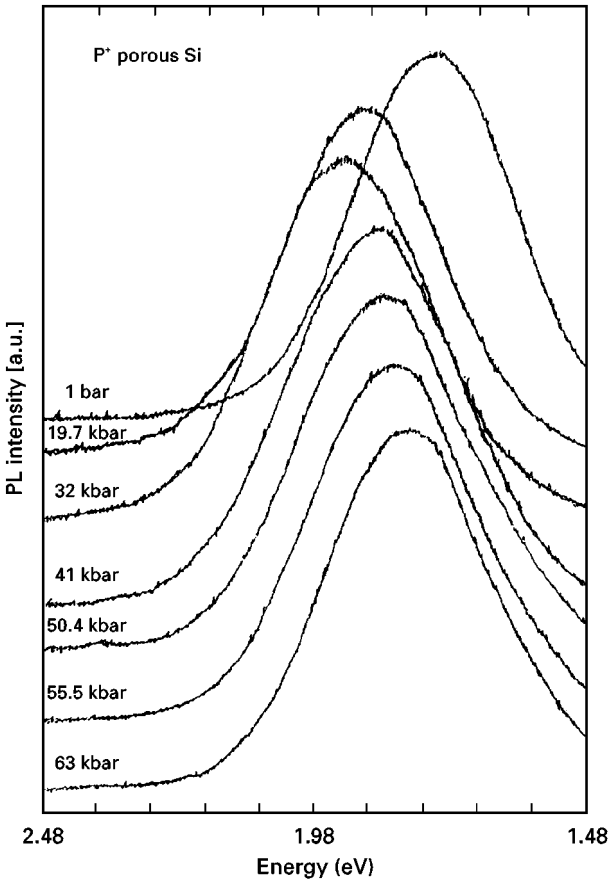

Figure 16 The PL spectra of a p^+ porous Si under several pressures.

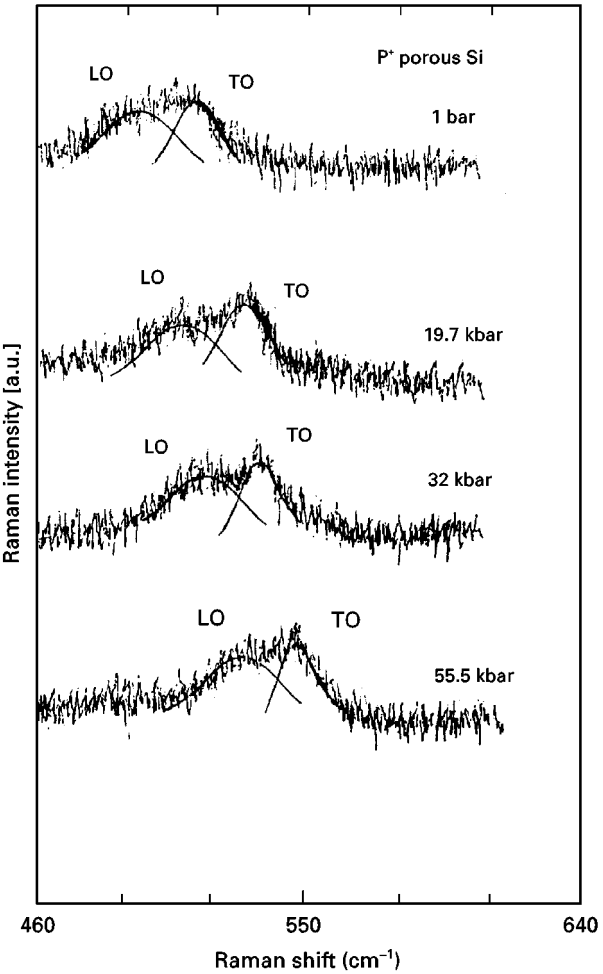

Figure 18 The Raman spectra for p^+ porous silicon at several pressures. The Raman spectrum is fitted with LO and TO peaks. The pressure behaviour of the Raman spectra show that the applied pressure only has a little effect on the residual strain in the Si particles of porous Si.

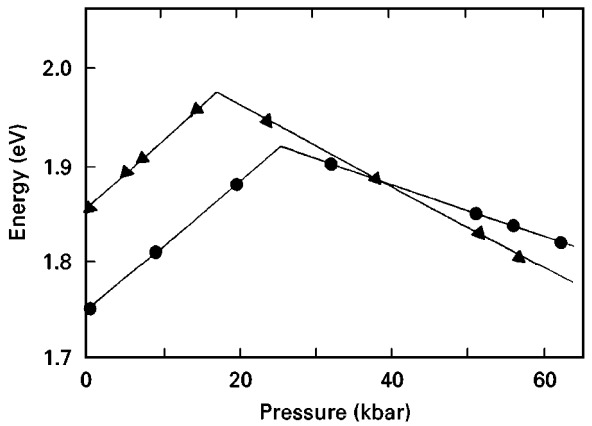

Figure 17 The pressure dependence of the PL peaks for p^+ (●) and p^- (▲) porous Si.

a pressure of 26 (17) kbar. At the higher pressure range, the peak energy decreases with pressure at the rate of -4.1 and -2.8 meV kbar^{-1} for the p^- and p^+ samples, respectively. A similar pressure rate, in the range -2.6 to -3.3 meV kbar^{-1}, was reported by others [59]. The strong pressure dependence of the PL peak of porous silicon shows that the emission mechanism of porous Si cannot be attributed to surface states or to any kind of deep defect states in porous Si, because the localized nature of deep defect states dictates that the binding energy of the defect states is insensitive to the applied pressure, as observed in GaP nanocrystals. There is no natural explanation for the pressure dependence of the PL in porous Si as anything other than a band-edge emission. In addition, the same results have been obtained using ethyl alcohol and pure water as the pressure-transmitting medium. This fact reflects that there was no chemical reaction between the transmitting medium and porous silicon.

Fig. 18 depicts Raman spectra of a p^+ porous silicon sample at several pressures. The TO and LO are red shifted from the normal triplet at $k = 0$ by 5 and 30 cm^{-1}, respectively. The pressure coefficient of the LO and TO peaks are 0.75 ± 0.5 and 0.60 ± 0.5 cm^{-1} kbar^{-1}, respectively. The pressure coefficient of the triplet modes from bulk Si is 0.52 cm^{-1} kbar^{-1}. From the Raman spectra of porous silicon under hydrostatic pressure, we can see that hydrostatic pressure has only a small effect on the residual strain in the porous silicon sample, although the applied pressure can constrain the strain induced by excitation. When the pressure is higher than 55 kbar, splitting of the LO and TO Raman peaks shows that there still exists more than 100 kbar uniaxial stress in the silicon particles of porous silicon. Clearly, the PL observed from porous silicon results from the lower energy level,

E^{3-6}. The pressure coefficient of the PL peaks for both samples should be close to $\frac{2}{3}\Xi_u(S_{11} - S_{12}) = 6.2\,\text{meV kbar}^{-1}$, which is in good agreement with the experimental results. The Stokes shift and band gap obtained from the cross-over pressure and pressure rate of the PL peaks are about 0.16 (0.11) and 1.9 (1.97 eV) for strained p^+ (p^-) porous Si, respectively. As the hydrostatic pressure is high enough to constrain the energy relaxation of the band edges (the cross-over pressure) completely, the band gap will decrease with a pressure rate of about $-1.5\,\text{meV kbr}^{-1}$ in bulk Si, provided that the six-fold degenerate conduction bands are not splitting, as is the case for GaP nanocrystals. However, there exists a fixed large [1 0 0] direction strain between the $E^{1,2}$ and E^{3-6} states in the strained silicon particles of porous silicon, as shown by the Raman spectra under pressure (Fig. 18). When the applied hydrostatic pressure is higher than the cross-over pressure, interaction between the $E^{1,2}$ and E^{3-6} states through the residual uniaxial strain will repel the lower energy level, E^{3-6}, down at a rate close to $-\frac{1}{3}\Xi_u(S_{11} - S_{12}) = -3.0\,\text{meV kbar}^{-1}$, which is basically consistent with the pressure rates obtained in this work and others [59].

In summary, we can conclude that the optical properties of porous silicon, in fact, result from strained silicon quantum dots. Both the formation mechanism and optical properties of porous silicon are naturally consistent with the CIDSE.

4. Conclusions

On the basis of experimental results on GaAs, GaP and Si nanocrystals, and porous silicon, we conclude that carrier-induced dynamic strain, or the lattice relaxation effect, is an intrinsic feature in solids, which plays an extremely important role in the electronic and optical properties of semiconductor nanocrystals. The dynamic strain induced by excited free carriers breaks the orthogonality of vibronic wave functions between excited states and the ground state, and, hence, relaxes the selection rule of crystal momentum conservation for optical transitions in a rigid nanocrystal. Therefore, the optical properties of semiconductor nanocrystals are dominated by multi-phonon-assisted electronic transitions.

The electron–phonon coupling mechanism for excited electrons at the conduction-band edge of a nanocrystal is dominated by deformation potential coupling through carrier-induced strain. The band-edge relaxation (or electron–phonon coupling strength) in a nanocrystal directly depends upon the pressure (or stress) rate of the band gap and the strain energy density produced by excitation. The direct-gap nanocrystals, which have high symmetry and large pressure coefficients for the band gap, such as GaAs nanocrystals, no longer show band-edge emission due to strong electron–long wavelength anharmonic acoustic phonon coupling. The band gap of GaAs nanocrystals will transfer from direct into indirect, with the X valleys as the lowest conduction-band edge, when the GaAs particle size is smaller than 5.0 nm.

The excited electrons at the degenerate valleys of an indirect-gap nanocrystal will induce a uniaxial strain, which, in turn, splits the degenerate levels into two groups, one group aligned along the strain (longitudinal) shifts to higher density, the other, perpendicular to the strain axis (transverse), is down shifted and becomes the lowest conduction-band edge. As a result, indirect-gap nanocrystals usually show two intrinsic emission bands; one of them results from higher energy unstable states, the other comes from energy-relaxed band edge states. The excited electrons at the indirect-band edge can couple with high energy acoustic and optical phonons at the corresponding edge of the phonon BZ. Compared with the direct-gap nanocrystals, indirect-gap nanocrystals usually exhibit fairly strong and broadened band-edge emission due to the shorter relaxation time of the excited electrons at the indirect-band edge. However, when carrier-induced strain is completely constrained by applied pressure, the optical transition in nanocrystals has to meet the selection rule of crystal momentum conservation. In this case, indirect-gap nanocrystals change back to poor emission materials, as in their bulk. The optical properties of porous Si are similar to those observed in Si nanocrystals. The light emission observed in porous Si, in fact, results from splitting lower energy E^{3-6} levels caused by the residual strain.

The large capture cross-section for a weak coupling deep centre can be achieved by band-edge relaxation of a nanocrystal. Consequently, deep centres in semiconductor nanocrystals usually show strong light emission, especially for nanocrystals with an indirect-gap or a direct-gap with a small pressure coefficient for the band gap, since the excited electrons at the conduction-band edge in these kinds of nanocrystals have relatively shorter relaxation times.

All vibrational modes in nanocrystals become soft compared with those in their corresponding bulk crystals, the degree to which depends on the strength of the carrier-induced strain. The selection rule of crystal momentum conservation for Raman scattering is relaxed by carrier-induced strain effects. Thus, first-order Raman scattering for some vibrational modes with $k \neq 0$ can become Raman active. The three-fold degenerate Γ optical modes in Si nanocrystals are split by carrier-induced [1 0 0] shear strain into a lower energy LO mode, with its eigenvector parallel to the strain direction, and higher energy doublet TO modes, with their eigenvectors perpendicular to the stress axis. It is worthwhile noting that since the conduction-band edge for nanocrystal systems is energy relaxed, the electron–phonon coupling strength measured by the PL spectrum is no longer the same as that measured by Raman scattering in nanocrystal systems.

Acknowledgements

The authors wish to thank Drs Richard D. Sarno, P. D. Persans and Robert H. Doremus for some helpful discussions; Dr J. Schroeder for partially supporting the experimental equipment and Mr Ray Dove for assistance in measuring particle size. This work was

partially supported by the National Science Foundation of China.

References

1. L. T. CANHAM, *Appl. Phys. Lett.* **57** (1990) 1046.
2. A. L. EFROS and A. L. EFROS, *Sov. Phys. Semicond.* **16** (1982) 772.
3. L. E. BRUS, *J. Phys. Chem.* **80** (1984) 4403.
4. *Idem. ibid.* **90** (1986) 2555.
5. Y. KAYANUMA, *Phys. Rev.* **B38** (1988) 9797.
6. Y. WANG, A. SUNA, W. MAHLER and R. KASOWSKY, *J. Chem. Phys.* **87** (1987) 7315.
7. A. P. ALIVISATOS, T. D. HARRIS, P. T. CARROLL, M. L. STEIGERWALD and L. E. BRUS, *ibid.* **90** (1989) 3463.
8. M. G. BAWENDI, W. L. WILSON, L. ROTHBERG, P. J. CARROLL, T. M. JEDJU, M. L. STEIGERWALD and L. E. BRUS, *Phys. Rev. Lett.* **65** (1990) 1623.
9. M. V. RAMA KRISHNA and R. A. FRIESNER, *J. Chem. Phys.* **95** (1991) 8309.
10. M. O. NEIL, J. MAROHN and G. McLENDON, *ibid.* **94** (1991) 8309.
11. K. I. KANG, A. D. KEPNER, S. V. GAPONENKO, S. W. KOCH, Y. Z. HU and N. PEYGHAMBARIAN, *Phys. Rev.* **B48** (1993) 15 449.
12. D. J. NORRIS and M. G. BAWENDI, *J. Chem. Phys.* **103** (1995) 5260.
13. X. S. ZHAO, Y. R. GE, J. SCHROEDER and P. D. PERSANS, *Appl. Phys. Lett.* **65** (1994) 2033.
14. S. H. TOLBERT and A. P. ALIVISATOS, *Science* **265** (1994) 373.
15. X. S. ZHAO, J. SCHROEDER, P. D. PERSANS and T. G. BILODEAU, *Phys. Rev.* **B43** (1991) 12 580.
16. A. P. ALIVISATOS, *Mater. Res. Bull.* **20** (1995) 23.
17. M. G. BAWENDI, P. J. CARROLL, W. L. WILSON and L. E. BRUS, *J. Chem. Phys.* **96** (1992) 946.
18. L. B'ANYAI, P. GILLIOT, Y. Z. HU and S. W. KOCH, *Phys. Rev.* **B45** (1992) 14 136.
19. H. RICHTER, Z. P. WANG and L. LEY, *Solid State Commun.* **39** (1981) 625.
20. X. S. ZHAO, Y. R. GE, J. SCHROEDER and P. D. PERSANS, *MRS Symp. Proc.* **358** (1995) 199.
21. X. S. ZHAO, P. D. PERSANS, J. SCHROEDER and Y. J. WU, *ibid.* **283** (1993) 127.
22. A. FRANCESCHETTI and A. ZUNGER, *Appl. Phys. Lett.* **68** (1996) 3455.
23. R. W. KEYS, *Solid State Phys.* **20** (1967) 37.
24. K. HUANG and A. RHYS, *Proc. R. Soc. Lond* **A204** (1950) 406.
25. K. HUANG, *Progress Phys.* **1** (1981) 31.
26. B. K. RIDLEY, "Quantum Processes in Semiconductors" (1982).
27. J. A. VANVECHTEN and C. D. THURMOND, *Phys. Rev.* **B14** (1976) 3539.
28. G. A. SAMARA and C. E. BARNES, *Phys. Rev. Lett.* **57** (1986) 2069.
29. R. A. SWALIN, "Thermodynamics of Solids" (1964).
30. J. BOURGOIN and M. LANNOO, "Point Defects in Semiconductors II, Experimental Aspects", 35, edited by M. Cardona, Springer Series in Solid-state Science (Springer).
31. J. SHAH and A. H. DAYEM, *Phys. Rev. Lett.* **37** (1976) 861.
32. O. B. WRIGHT and V. E. DAYEM, *Appl. Phys. Lett.* **66** (1995) 1190.
33. P. CALCOTT, K. NASH, L. CANHAM, M. KANE and D. BRUMHEAD, *J. Phys. Condens. Matter* **5** (1993) L91.
34. C. H. HENRY and D. V. LANG, *Phys. Rev.* **B15** (1977) 989.
35. C. E. BARNES and G. A. SAMARA, *Appl. Phys. Lett.* **43** (1983) 677.
36. I. BALSLEV, *Phys. Rev.* **143** (1996) 636.
37. M. F. LI, X. S. ZHAO, Z. Q. GU, J. X. CHEN, Y. J. LI and J. Q. WANG, *ibid.* **B43** (1991) 14 040.
38. E. ANASTASSAKIS, A. PINCZUK, E. BURSTEIN, F. H. POLLAK and M. CARDONA, *Solid State Commun.* **8** (1970 133.
39. F. CERDEIRA, C. J. BUCHENAUER, F. H. POLLAK and M. CARDONA, *Phys. Rev.* **B5** (1972) 580.
40. Z. H. LEVINE, H. ZHONG, S. WEI, D. C. ALLAN and J. W. WILKINS, *ibid.* **B45** (1992) 4131.
41. G. L. BOTTGER and C. V. DAMSGARD, *J. Chem. Phys.* **57** (1972) 1215.
42. C. A. ARGUELLO, D. L. ROUSSEAU and S. P. S. PORTO, *Phys. Rev.* **181** (1969) 1351.
43. O. GUNNARSSON, *Rev. Mod. Phys.* **69** (1997) 575.
44. W. A. SAUNDERS, R. B. LEE, H. A. ATWATER, K. J. VAHALA, R. C. FLAGAN and P. C. SERCEL, *MRS Symp. Proc.* **283** (1993) 771.
45. A. YACOBY, M. HEIBLUM and D. H. SHTRIKMAN, *Phys. Rev. Lett.* **74** (1995) 4047.
46. M. VOLLNER, E. J. MAYER, W. W. RUHLE, A. KURTENBACH and K. EBERL, *Phys. Rev.* **B54** (1996) R17 292.
47. M. R. SILVESTRI and J. SCHROEDER, *ibid.* **B50** (1994) 15 108.
48. C. PATEL, T. J. PARKER, H. JAMSHIDI and W. F. SHERMAN, *Phys. Status Solidi* **B122** (1984) 461.
49. L. L. CHASE, W. HAYES and J. F. RYAN, *J. Phys. C, Solid State Phys.* **10** (1977) 2957.
50. W. A. HARRISON, *Phys. Rev.* **B10** (1974) 767.
51. G. H. LI, X. S. ZHAO, H. X. HAN, Z. P. WANG, R. M. TANG and J. Z. HU, *Chinese J. Semiconduct.* **5** (1984) 558.
52. G. BURNS and B. A. SCOTT, *Phys. Rev. Lett.* **25** (1970) 1191.
53. Q. ZHANG, S. C. BAYLISS and D. A. HUTT, *Appl. Phys. Lett.* **66** (1995) 1977.
54. S. VEPREK, Z. IQBAL, H. R. OSTWALD and A. P. WEBB, *J. Phys.* **C14** (1980) 295.
55. T. R. HART, R. L. AGGARWAL and B. LAX, *Phys. Rev.* **B1** (1970) 638.
56. S. GARDELIS, U. BANGERT and B. HAMILTON, *Thin Solid Films* **255** (1995) 167.
57. J. D. LECUYER and J. P. G. FARR, *MRS Symp. Proc.* **283** (1993) 3.
58. P. KOCH, T. MUSCHIK, D. I. KOVALEV, F. KOCH and V. LEHMANN, *MRS Symp. Proc.* **283** (1993) 179.
59. A. K. SOOD, K. JAYARAM, D. VICTOR and S. MUTHU, *J. Appl. Phys.* **72** (1992) 4963.

Received 9 April
and accepted 22 June 1998